Development of molecularly imprinted polymer (MIP)-based microfluidic gas sensors for Tetrahydrocannabinol (THC) detection

By

Peyman Azhdary

B.Sc., Iran University of Science and Technology, Iran, 2019

A Thesis Submitted in Partial Fulfillment of the

Requirements for the Degree of

Master of Applied Science

in the Department of Mechanical Engineering

University of Victoria

We acknowledge and respect the lək̓ʷəŋən peoples on whose traditional territory the university stands and the Songhees, Esquimalt and W̱SÁNEĆ peoples whose historical relationships with the land continue to this day.

Supervisory Committee

Development of molecularly imprinted polymer (MIP)-based microfluidic gas sensors for Tetrahydrocannabinol (THC) detection

By

Peyman Azhdary

B.Sc., Iran University of Science and Technology, Iran, 2019

Supervisory committee

Dr. Mina Hoorfar, Supervisor
Department of Mechanical Engineering

Dr. Stephanie Willerth, Departmental Member
Department of Mechanical Engineering

Abstract

Molecularly imprinted polymers (MIPs) are synthetically fabricated materials capable of selectively binding with target analytes and thereby enabling their selective detection. MIPs are good candidates for the selective detection of Tetrahydrocannabinol (THC), the primary psychoactive ingredient in Cannabis, as there is an emergent need for new technologies to selectively detect and monitor THC for health, safety, and quality control applications, especially portable miniaturized devices (e.g. for roadside tests). Microfluidic gas sensors are modifiable miniaturized devices that selectively detect a target gas through microchannel modifications. In this study, highly selective microfluidic gas sensors toward THC are reported based on MIP coatings. The sensors' performance was evaluated by exposure to THC, Cannabidiol (CBD), methanol, and ethanol samples. The findings demonstrated that the recognition sites of MIP properly captured THC molecules, enabling distinguishing THC from CBD, methanol, and ethanol.

Table of Contents

Supervisory Committee ..... **ii**

Abstract ..... **iii**

Table of Contents ..... **iv**

List of Figures ..... **vii**

List of Tables ..... **x**

Acknowledgements ..... **xi**

Dedication ..... **xii**

Chapter 1: Introduction **1**

1.1 Molecularly imprinted polymers (MIPs) 1

1.2 Methods of synthesis of MIPs 2

1.2.1 Precipitation polymerization 2

1.2.2 Electrochemical polymerization 3

1.2.2.1 Procedure of electrosynthesis of MIPs 3

1.2.2.2 The monomer in electropolymerized MIPs 4

1.2.2.3 Monomer and template ratio 5

1.2.2.4 Advantages and disadvantages of electrosynthesis technique 5

1.3 Application of MIPs in the sensors field 6

1.3.1 Fabrication of MIP electrochemical sensors 9

1.3.2 MIPs and microfluidic gas sensing 9

1.4 Δ9-tetrahydrocannabinol (Δ9-THC) importance 11

1.5 Objective 13

Chapter 2: Methodology 14

2.1 Microfluidic channels along with MOS sensors 14

2.2 MIP thin film synthesis 15

2.3 MIP NPs synthesis 17

2.4 MIP and NIP thin film coated channels 18

2.5 MIP and NIP NPs coated channels 19

2.6 Microchannel and NPs Characterization 19

2.6.1 Scanning electron microscopy (SEM) 19

2.6.2 X-ray Photoelectron Spectroscopy (XPS) 20

2.6.3 Raman spectroscopy 20

2.7 Response Analysis 20

2.8 Principal Component Analysis (PCA) 21

2.9 Test setup and data capturing 22

Chapter 3: Results and discussion 24

3.1 Characterization results 24

3.1.1 MIP and NIP NPs SEM 24

3.1.2 MIP and NIP NPs Raman Spectroscopy 25

3.1.3 MIP and NIP thin film coated microchannels SEM 26

3.1.4 MIP and NIP thin film coated microchannels XPS 27

3.2 Gas sensing results 29

3.2.1 MIP and NIP NPs coated channels 29

3.2.2 MIP and NIP thin film coated channels 34

3.3 Statistical Analysis 41

3.4 Classification 42

Chapter 4: Conclusion and future works 45

4.1 Conclusion 45

4.2 Future works 46

Bibliography 49

List of Figures

Figure 1 - Microfluidic channel and MOS sensor 14

Figure 2 - Microchannel a) before and b) after MIP thin film coating 16

Figure 3 - a) Polymerization in oil bath. b) Product. 17

Figure 4 - Experimental setup for gas sensing tests and data capturing 23

Figure 5 – a) SEM image and b) size distribution of MIP NPs 24

Figure 6 - a) SEM image and b) size distribution of NIP NPs 25

Figure 7 - Raman spectra of imprinted MIP NPs, extracted MIP NPs, and NIP NPs 26

Figure 8 - SEM images of surface a) before and b) after MIP thin film coating 27

Figure 9 - XPS results of a) 3dprinted surface b) Parylene C coated surface c) Gold coated surface, and d) MIP thin film coated surface 28

Figure 10 - a) NIP NPs channel's MOS sensor resistance change upon exposure to 600 ppm of four different analytes. b) NIP NPs channel's MOS sensor resistance change for four consecutive cycles of exposure to 600 ppm of THC. C) The calibration curve (the sensor relative response versus the concentration of the analyte) for NIP NPs channel exposed to four analytes. d) The PC1 and PC2 presentation of different analytes for NIP NPs channel. 31

Figure 11 - a) MIP NPs channel's MOS sensor resistance change upon exposure to 600 ppm of four different analytes. b) MIP NPs channel's MOS sensor resistance change for four consecutive cycles of exposure to 600 ppm of THC. C) The calibration curve (the sensor relative response versus the concentration of the analyte) for MIP NPs channel exposed to four analytes. d) The PC1 and PC2 presentation of different analytes for MIP NPs channel. 32

Figure 12 – The resistance versus time graphs for two channels upon exposure to five different concentrations (300 ppm–700 ppm) of a) THC, b) CBD, c) ethanol, d) methanol. 33
Figure 13 - a) NIP thin film channel's MOS sensor resistance change upon exposure to 300 ppm of four different analytes. b) NIP thin film channel's MOS sensor resistance change for four consecutive cycles of exposure to 300 ppm of THC. C) The calibration curve (the sensor relative response versus the concentration of the analyte) for NIP thin film channel exposed to four analytes. d) The PC1 and PC2 presentation of different analytes for NIP thin film channel. 36
Figure 14 - a) MIP thin film 1 channel's MOS sensor resistance change upon exposure to 300 ppm of four different analytes. b) MIP thin film 1 channel's MOS sensor resistance change for four consecutive cycles of exposure to 300 ppm of THC. C) The calibration curve (the sensor relative response versus the concentration of the analyte) for MIP thin film 1 channel exposed to four analytes. d) The PC1 and PC2 presentation of different analytes for MIP thin film 1 channel. 37
Figure 15 - a) MIP thin film 2 channel's MOS sensor resistance change upon exposure to 300 ppm of four different analytes. b) MIP thin film 2 channel's MOS sensor resistance change for four consecutive cycles of exposure to 300 ppm of THC. C) The calibration curve (the sensor relative response versus the concentration of the analyte) for MIP thin film 2 channel exposed to four analytes. d) The PC1 and PC2 presentation of different analytes for MIP thin film 2 channel. 38
Figure 16 - a) MIP thin film 3 channel's MOS sensor resistance change upon exposure to 300 ppm of four different analytes. b) MIP thin film 3 channel's MOS sensor resistance change for four consecutive cycles of exposure to 300 ppm of THC. C) The calibration curve (the sensor relative response versus the concentration of the analyte) for MIP thin film 3 channel exposed to

four analytes. d) The PC1 and PC2 presentation of different analytes for MIP thin film 3 channel. 39

Figure 17 - The resistance versus time graphs for two channels upon exposure to five different concentrations (300 ppm–700 ppm) of a) THC, b) CBD, c) ethanol, d) methanol. 41

Figure 18 – a) Classification accuracy versus the number of used principal components, and b) The confusion matrix when the combined data from MIP and NIP NPs channels were used for the classification..... 43

Figure 19 - a) Classification accuracy versus the number of used principal components, and b) The confusion matrix when the combined data from MIP thin film 2 and NIP thin film channels were used for the classification..... 44

Figure 20 - Elbow curve for a) NPs coated channels data and b) thin film coated channels data 44

List of Tables

Table 1 - XPS results including peaks and row area 28

Acknowledgements

I would like to express my highest gratitude to my supervisor, Dr. Mina Hoorfar, for her support throughout this study. I would like to thank all of our lab researchers, especially Nishat Tasnim, Dr. Sajjad Janfaza, Mahan Ghazi, and Dr. Somayeh Fardindoost for their help and assistance.

We acknowledge and respect the lək̓ʷəŋən peoples on whose traditional territory the university stands and the Songhees, Esquimalt and W̱SÁNEĆ peoples whose historical relationships with the land continue to this day.

We acknowledge and respect the Syilx Okanagan Nation and their peoples, in whose traditional, ancestral, unceded territory UBC Okanagan is situated.

Dedication

To my parents for their endless love, support, and encouragement

Chapter 1: Introduction

1.1 Molecularly imprinted polymers (MIPs)

The molecular imprinting technique is a useful tool for creating durable materials with specific recognition features [1]. Molecularly imprinted polymers (MIPs) are a new class of materials with synthetically produced receptor architectures capable of selective binding [2]. Even when present in complex mixtures, the resulting polymer, which is highly crosslinked and durable, can identify and selectively bind the template [3].

Typically, molecular imprinting is defined as the creation of a particular recognition cavity by the polymerization of functional monomers and a crosslinker around a template [4]. A template and a functional monomer first combine to create a complex. Second, a crosslinker is used to obtain a successful polymerization all around the complex. After the template molecule is extracted, the recognition cavity is created. Recognition cavities can specifically interact and bind with the target molecule since they resemble it in terms of size, shape, and functional group. In other words, a lock and key mechanism exists in which the target analyte serves as the "key," and MIP serves as the "locks" that fit it perfectly [5]. There is a growing interest in leveraging MIP technology for sensing application and a key research topic has been the synthesis of MIPs with improved binding capacity, imprinting factor, and selectivity towards target analytes. MIPs have superior or comparable high affinity and selectivity compared to natural receptors (such as antibodies) [6]. MIPs may be fabricated for a wide range of chemical and biological species [7]. Strong cross-linking in these polymers also provides high chemical, mechanical, and thermal resistance, allowing MIPs to be used in challenging chemical environments [7]. These environments include those that are acidic, alkaline, or include organic solvents. In addition, MIPs production is low

cost, and they are generally resistant to high pressure and temperature conditions [7] resulting in their binding cavities can retain their selectivity even after prolonged storage [7].

1.2 Methods of synthesis of MIPs

Various methods, such as bulk polymerization, precipitation polymerization, suspension polymerization, emulsion polymerization, radical polymerization, core-shell polymerization, and electrochemical polymerization, have been developed for the synthesis of MIPs. Other recent and less conventional production methods of MIPs and MIP composites are soft lithography or surface stamping and phase inversion.

1.2.1 Precipitation polymerization

An effective approach for creating the spherical molecularly imprinted polymer is precipitation polymerization. This technique involves dissolving template molecules and functional monomers in a suitable solvent. After adding a certain quantity of cross-linker and initiator, the polymerization is carried out using light or heat. Precipitation polymerization needs a long reaction time, and a suitable solvent is used to wash away the template molecule from the polymer precipitate at the end. The solvent in the precipitation polymerization must meet certain requirements in order to dissolve the target molecules, functional monomer, cross-linker, and initiator while leaving the produced MIPs unaffected [8]. Because surfactants are not used for this synthesis, less environmental pollution results. Additionally, the size distribution of the synthesized polymer particle is uniform. Some drawbacks of this approach include the large solvent volume, lengthy reaction time, and challenging solvent removal from the polymer [9]. This method has been successfully used for the synthesis of polymethyl methacrylate nanoparticles with acetone recognition sites [10] and Creatinine MIP nanoparticles [11].

1.2.2 Electrochemical polymerization

The synthesis of a polymer on the surface of a solid electrode material and/or a supporting substrate material is the fundamental idea behind electropolymerization or electrochemical polymerization [12]. It is a technique for creating polymer films under the influence of an electric field, and this technique enables the direct deposition of an MIP film onto a transducer, such as an electrode [13]. For example, it can be done on an electrode of a resonator of a quartz crystal microbalance (QCM) or a chip for surface plasmon resonance (SPR) spectroscopy measurements [14]. In electropolymerization, a conductive MIP polymer layer is applied to an electrode or a supporting substrate while the desired template is present. A three-electrode experimental setup is needed for electropolymerization. These three electrodes are the working, reference, and counter electrodes. The working electrode is covered with a MIP film [15]. In a standard three-electrode electropolymerization experimental setup, it is the electrode where the polymerization occurs. It can be a conducting glass, a noble metal, a carbon substance, or an alloy. A reference electrode, most often an Ag/AgCl electrode or a saturated calomel electrode (SCE), enables the working electrode surface to be adjusted to a known potential. The electrical circuit in the electrochemical cell is then closed by the counter electrode, which is often a platinum or nickel rod. The template molecule, the monomer, the supporting electrolyte, and the solvent are all present in the solution that these three electrodes are submerged [12].

1.2.2.1 Procedure of electrosynthesis of MIPs

The chosen monomer and the template are combined in a solution at a predetermined ratio to begin the electrosynthesis of MIPs by electropolymerization. The electropolymerization is carried out once they have been combined [12]. Different electrochemical methods may be employed to electropolymerize MIPs; the most popular ones are potentiostatic [16], galvanostatic

[17], or potentiodynamic [18] procedures. A constant potential is used to carry out the earlier method (potentiostatic). A constant current drives the process of galvanostatic polymerization. The cyclic voltammetry technique, which is used in the potentiodynamic method, involves sweeping across a certain window of potentials. After the production of polymer layers in which the template molecule is trapped, the polymer is put through an extraction phase by submerging the working electrode in an extraction solution that leaves behind cavities which contain imprints of the selected template [12].

1.2.2.2 The monomer in electropolymerized MIPs

The electropolymerization process and the effectiveness of the electrosynthesized MIPs are significantly influenced by the monomer choice. The monomer should have the ability to interact with the template in addition to being electroactive [12]. The monomer creates a complex with the template, and it is crucial to carefully choose the functional monomer since it should provide the necessary functional groups. When the template and functional monomer interact more strongly, a more stable complex with a high capacity for binding is formed, which improves the cavities' capacity for recognition and selectivity [19]. Pyrrole [20], [21], aniline [22], [23], o-phenylenediamine [24], and carbazole [25] are among the popular monomers that have been used to create MIPs and MIP composites. Many researchers employed pyrrole to electrochemically produce MIPs, making it one of the most widely used monomers. This monomer is the subject of much attention due to its easy oxidation and water solubility. Additionally, polypyrrole has a variety of advantageous inherent qualities, including great biocompatibility, environmental stability, superior redox characteristics, and the potential to have high electrical conductivity [26], [27].

1.2.2.3 Monomer and template ratio

The quantity and quality of the MIPs unique recognition sites are dependent on the molar ratio of the template to the functional monomer. In general, the self-assembly of the template molecule to functional monomers may be made simple and completely accomplished by increasing the ratio of the function monomer to the template molecule. However, a large fraction of functional monomer may allow for self-aggregation. This increases the nonselective binding sites produced by functional monomer residues that are still in the unassembled state of the polymer. The problem of low functional monomer is the lack of functional monomer resulting in less than ideal assembly [28]–[30].

1.2.2.4 Advantages and disadvantages of electrosynthesis technique

Comparing electropolymerization to conventional methods, there are various benefits. For instance, it enables the polymer to adhere to the transducer surface more effectively. Furthermore, the MIPs may be produced using the electropolymerization approach in a matter of minutes. The ability to produce MIPs for proteins, bacteria, and viruses in an aqueous environment and at room temperature is a significant benefit [12]. Additionally, the choice of an appropriate solvent and supporting electrolyte allows for control over the polymer's shape and layer thickness (by regulating the amount of charge transmitted during electropolymerization) [15]. A polymerization initiator, UV light, or heating is not required in this process [26]. The creation of MIPs or MIP composites using electropolymerization processes is compatible with the development of sensors and especially electrochemical sensors. However, the electrosynthesis method requires fresh synthesis as the electrode's effectiveness declines over time, which has an adverse effect on the lifespan of the produced MIPs [12].

1.3 Application of MIPs in the sensors field

The production of transducers, sensors, and delivery systems has been revolutionized by MIPs because of their exceptional durability, stability, affordability, a wide range of applications, and adjustability for different applications [13]. Drug delivery, separation sciences, sensors and biosensors, food analysis, wastewater treatment, purification, and catalysis are some of the notable application fields for MIPs.

Generally, sensors are analytical devices that may be used to detect the concentration of various analytes of interest. The employment of electrochemical and optical sensors has been more popular owing to their experimental simplicity, broad applicability, cheap cost, and imitation recognition function toward target molecules [31]. The main components of a sensor are the molecule identification component and the and signal converter. The basic principle of detection based on the use of the molecule-identification element (receptor) to selectively identify a target analyte and then use a signal converter (transducer) to generate an output signal [32]. To enhance the sensitivity and selectivity of sensors, they are often modified with various chemical substances such as carbon nanomaterials [33], enzymes [34], aptamers [35], antibodies [36], and quantum dots [36].

MIPs are often utilized in the construction of sensors in order to improve their analytical performance, particularly selectivity [37]. The response of sensors to the selective binding of target molecules to the MIP interface is used to detect the presence of the target analyte in samples. Several transduction methodologies are applicable for MIP sensing, such as a change in electrical current in electrochemical sensors, a shift in fluorescence intensity in quantum dot sensors, a shift in angle or wavelength in surface plasmon resonance sensors, and changes in oscillation mode in piezoelectric sensors are all brought on by the binding event [38].

Si et al. described the use of MIPs in the creation of electrochemical sensors for the detection of various neurotransmitters. For the MIP sensor, pyrrole (PPy) and o-phenylenediamine (o-PD) were employed as functional monomers. Using differential pulse voltammetry (DPV) on three separately constructed custom-built MIP-based sensors, they show the capability of selective detection of dopamine (DA), norepinephrine (NE), and epinephrine (EP). Through testing, they found that all MIP sensors were more sensitive than non-imprinted (NIP) sensors because of their specialized molecular receptors [39].

Hawari et al. showed the production and properties of a fruit volatile imprinted polymer, and a novel technique for determining fruit ripeness based on MIP-QCM was presented by them. MIPs with templates such as limonene, α-pinene, and β-pinene were synthesized and coated onto the surface of QCMs (Quartz Crystal Microbalances). The MIP-QCM sensors used to specifically detect targeted volatiles from mango [40].

MIP materials can be further modified to create novel composites and custom sensor architectures with enhanced features [41]. MIP composites and MIP nanocomposites may be fabricated using a wide variety of materials and customized based on the specific application. As an example, Mousazadeh et al. developed a chemiresistive sensor for the detection of hexanal, a volatile organic molecule that has been shown to be a biomarker for cancer, using a nanocomposite of gold nanoparticles (AuNPs) and hexanal imprinted MIPs. The sensor's electrical response and resistance change were measured after drop-casting the nanocomposite onto an interdigitated electrode. The linear range of the sensor was estimated to be between 2.5 and 300 ppm, while the limit of detection was found to be 1.1 ppm. In a test of selectivity, the sensor's response to hexanal was three greater compared to other volatile organic compounds with a similar number of carbon atoms [42]. Similarly, Jahangiri-Manesh et al. described the development of a chemiresistive

sensor for selective acetone gas detection using a composite of MIPs and AuNPs. The limit of detection (LOD) was 66 ppm, and the reaction time was 3.7±1 s [43].

Janfaza et al. presented a chemiresistive sensor for the lung cancer biomarker hexanal. MIP nanoparticles and multi-walled carbon nanotubes were combined to create a composite material to be used in the sensor. The detection limit was 10 ppm, and the sensor was effective throughout a concentration range of 10 to 200 ppm [44].

Because of the advantages mentioned for MIPs, these kinds of sensors have become commercially attractive, especially when selectivity is of utmost importance. Some of the most promising MIP sensor application fields are 1) in the production of chemicals and pharmaceuticals under harsh circumstances such as high and low pH, hazardous solvents, high temperature, pressure, and radiation, 2) in medicine and pharmacology for in vivo monitoring and drug screening 3) in continuous emissions sensors, remote sensing, and point-source monitors for the environmental applications 4) in the investigation of harsh conditions in deep space and space exploration [45].

However, before effective commercialization can begin, several major issues related to MIP development must be resolved. These include the creation and verification of a universal MIP design protocol, the creation of MIPs that can work well in water, establishing of efficient immobilization procedures, and enhancing the ratio of specific to nonspecific binding and significantly boosting polymer affinity [45]. Polymer chemists building MIPs and engineers creating sensors need to communicate more effectively. As technology develops further, MIP sensors will occupy distinct market niches.

1.3.1 Fabrication of MIP electrochemical sensors

MIP electrochemical sensors are fabricated by mounting MIP to the electrode surface to work as the selective recognition element of the sensor. The electrochemical signals generate when MIPs detect the target analyte, and electrochemical sensing occurs. The Electropolymerization method has been successfully used to fabricate these MIP electrochemical sensors. In this method, MIP is electropolymerized on an electrode in the presence of a template and after the extraction step, specific recognition cavities exist within the polymer matrix that are complementary in size and form to the template. This synthesis method of MIPs on the electrodes has overcome the difficulties and obstacles of conventional methods [46]. This approach is excellent for the creation of sensors, and it accurately synthesizes a sensitive layer on the surface of an electrode using a deposition procedure [47].

1.3.2 MIPs and microfluidic gas sensing

The most popular techniques for the detection of gases include gas chromatography, optical techniques, surface acoustic wave (SAW) techniques, and chemiresistive techniques [48]–[54]. The working principle of chemiresistive gas sensors is based on conductivity changes when the sensing material is exposed to the target gas. One of the most popular gas detectors operating based on this working principle is the Metal Oxide Semiconductor (MOS) sensors. Different geometries of MOS sensors may be created, ranging from bulk samples to nanostructures like nanorods [55], nanosheets [56], and nanowires [57]. For a particular application, these sensing layers may be chemically and physically modified.

Excellent electrochemical and sensing capabilities may be found in metal oxides [58]. Chemical and gas sensors have utilized oxides of different metals as their primary recognition components since 1962 [59]–[62]. Metal oxides are well suited for use as sensors due to their low

cost, great chemical, and thermal stability, outstanding mechanical and electrical qualities, and compatibility with a range of electronic, optical, gravimetric, and acoustic equipment [63].

Many different gases, including volatile organic compounds, hydrogen sulfide (H_2S), ammonia (NH_3), nitric oxides (NOx), and other nuisance gases have been detected using metal oxide semiconductors. For example, Ghimbeu et al. developed a metal-oxide-semiconductor (MOS) gas sensor for H_2S using tin oxide doped with copper oxide (Cu - SnO_2) sheets. At a relatively low working temperature (100 °C), this sensor showed a strong response to concentrations as low as 10 ppm of H_2S, demonstrating both high sensitivity and selectivity [79].

When it comes to detecting different molecular targets in complex mixes or actual samples, metal oxides have low and poor selectivity [64].To enhance the selectivity of these MOS sensors, they can be integrated with a microfluidic channel. The channels can be 3d-printed in different geometries, dimensions, surface chemistries, and with/without microfeatures to improve the selectivity of detection. The diffusion and adsorption /desorption of the analyte molecules along the channel, which are affected by the channel coating and dimensions, provide us with a more selective detection [65]–[67]. Adjustment of the channel coating and the combination of the layers should be observed [68]. The coating and roughness of the channel can be changed in different ways (e.g., by adding nanostructures [69]). Also, the presence of micro features in the channel in an optimized way (optimized dimensions and distance between each other) improves the selectivity of this gas detector [70].

Different coatings can be applied on the surface of these channels based on their application. Coating channels with MIPs is a novel sensing technique based on the selective trapping of a target analyte and thereby preventing its diffusion through the microchannel [71]–[73]. In this way, the incorporation of MIPs into the channel can be modify its surface properties

and interaction with the analyte. A differential signal based on MIPs and NIPs can accurately signal the presence of the MIP-targeted analyte. Janfaza et al. previously combined a 3D-printed microfluidic channel with MIP NPs to develop a dual channel device for selective detection of acetone [10].

1.4 Δ9-tetrahydrocannabinol (Δ9-THC) importance

Cannabis products are used widely as a textile, food, and recreational and medicinal drugs [74]. About 3.9% of the world's adult population, or 192.2 million individuals (aged 15–64), used cannabis in 2016, according to a study by the United Nations Office on Drugs and Crime (UNODC) [75]. These indicate a demand for expanding cannabinoids-related knowledge. The rising public pressure in favor of cannabis legalization has also had an impact on the expanding scientific interest in cannabis research. Peer-reviewed Cannabis research publications rose annually by an average of 13% between 1990 and 2016, over that time period, and there were 93 research publications on cannabis published in total in 1990, compared to 2161 articles in 2016 (as observed on Google Scholar and PubMed with cannabis and synonyms thereof as search terms) [76].

Two of the most important cannabinoids are Δ9-THC and cannabidiol (CBD). Δ9-THC is the main psychoactive component of Cannabis, influencing brain function and impairment [77]–[79]. For recreational usage, cannabis with a high amount of Δ9-THC, the major psychoactive component, is preferred over CBD which is better known for its medicinal uses and lack of psychoactivity [80]. CBD and Δ9-THC have similar molecules with totally different impacts and applications. Therefore, it is important to be able to distinguish a Δ9-THC sample from a CBD sample. Despite the fact that cannabinoid sensing procedures are well established in laboratory-

based approaches, miniaturized and portable cannabis sensors are not yet widely developed [81]. Various methods, such as gas chromatography-mass spectrometry (GC-MS) and high performance liquid chromatography (HPLC), have been employed to measure Δ9-THC and its respective metabolites, such as 11-hydroxy-Δ9-THC (11-OH-Δ9-THC) and 11-nor-9-carboxy Δ9-THC (Δ9-THCCOOH) in different biological matrices, and MIPs can be considered as good candidates to be integrated with sensing devices and methods to improve the selectivity toward Δ9-THC. Δ9-THC MIP sensors can be considered as useful platforms for different applications, especially those requiring miniaturized devices such as roadside tests and extraction technologies. It should be noticed that for such applications, the device needs to detect concentrations as low as 50 ppb (ideally 250 ppt for breath analysis) [76].

A micro-solid extractor for cannabinoids using MIPs and a high performance liquid chromatography-tandem mass spectrometry (HPLC-MS/MS) system was described in analyzing the plasma and urine of marijuana abusers by Sanchez-Gonzalez et al. [82].

Nestic et al. described using MIP coupled with GC-MS to extract tetrahydrocannabinol and its main metabolites in urine samples [83].

Zhang et al. showed the development of a series of carbon-based sensors using carbon materials and THC-imprinted poly(MAACo-EGDMA). High THC selectivity was acquired using molecular imprinting technique. The huge surface areas of carbon materials provided efficient detection [84].

1.5 Objective

Selective detection of different cannabinoids and the capability to distinguish them from each other is a challenging and important goal. THC, the primary psychoactive component of Cannabis, is needed to be differentiated from other cannabinoids, especially CBD which has similar chemical formula and structure to THC without any psychoactive effects. There is an emergent need for the portable miniaturized devices with this capability. Developing this kind of device can result in fabrication of THC detection devices for roadside tests, quality control tests in extraction technologies, and many other applications. Here, the feasibility of the integration between MIPs and microfluidic gas sensors for the selective detection of THC is studied. The MIP's and microfluidic gas sensors' characteristics and the ease of control on the properties of the resulting device make it an ideal choice for the aforementioned applications. The development of this device results in a portable, compact, relatively cheap, sensitive, and highly selective device toward THC.

Chapter 2: Methodology

2.1 Microfluidic channels along with MOS sensors

Three main parts form the microfluidic gas sensor; 1) 3D-Printed microchannel, 2) MOS sensor, 3) Electrical circuit [85], [86]. A connex 500 3D printer was used to fabricate the optimized microfeatures embedded microchannels from VeroClear RGD810 [67], [87] with the dimensions of 500 μm, 3 mm, and 3 cm as the height, width, and length, respectively. The microfeatures' size and distribution are very important. 50 microfeatures were added to the microchannel with a radius of 0.35 mm, a height of 0.4 mm, and distance of 0.8 mm. This microchannel has been developed in previous studies [70]. The microfluidic gas sensor's selectivity is improved by the high surface-to-volume ratio (MC_s/MC_v) of the microchannel, which enhances the surface interaction between the target analytes and microchannel [88], [89]. The microchannel and MOS sensor can be seen in Figure 1.

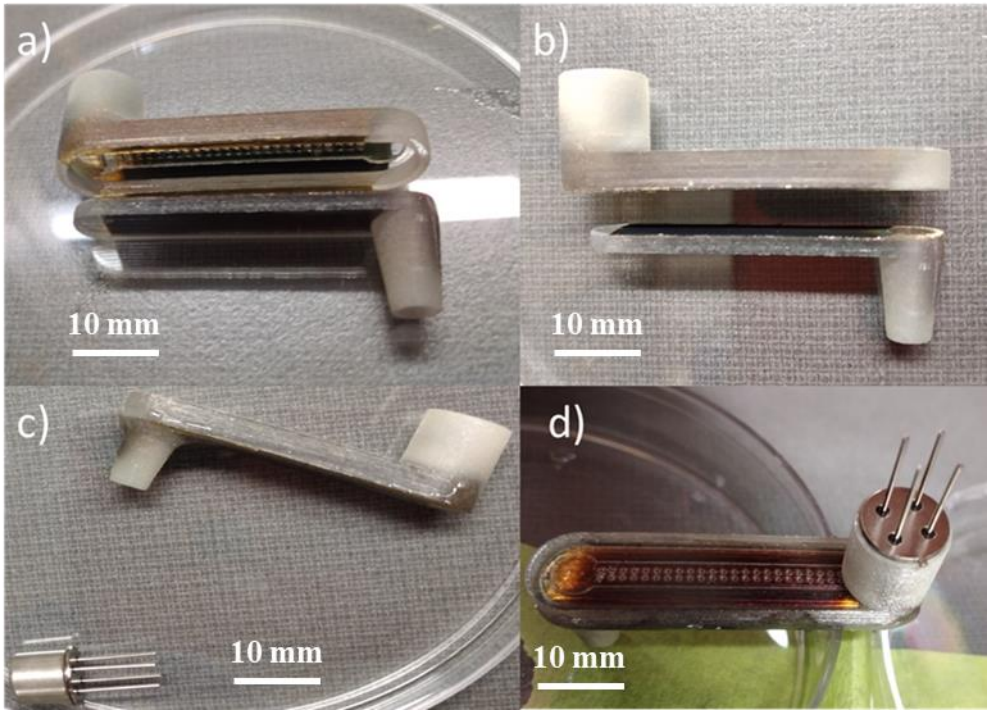

Figure 1 - Microfluidic channel and MOS sensor

Parylene C, with a thickness of 5 microns, was coated on the channels using a chemical vapor deposition (CVD) coating machine (SCS PDS 2010 Labcoater) to create a barrier layer that is chemically inert. The figaro MOS sensor connected to the electrical circuit was put at one end of the channel, and the gas entered the channel from the other end during the exposure time. The analytes diffuse along the channel and reach the sensor. When the target analyte reaches the sensing layer of a MOS sensor, the sensing layer's conductivity and the signal are altered. The MOS sensor is connected to the electrical circuit and a 5-volt DC power source (VC) to get the required power for reading the response signals from the sensor and work with the ideal working temperature (300º C) maintained by the sensor's microheater.

2.2 MIP thin film synthesis

Electropolymerization synthesis is used in this study. To begin the electrosynthesis of MIPs by electropolymerization, the template (THC) and the selected monomer (pyrrole) were mixed in a solution at a specified ratio. There are three different ratios that were investigated in this study. They are 20:1, 6:1, and 2:1 (monomer: template). After they mixed, sodium perchlorate monohydrate (0.1 M) was added to the mixture as the electrolyte to enhance the conductivity of the solution. The electropolymerization requires a three-electrode experimental setup. Working, reference, and counter electrodes are these three electrodes, and they are submerged in the prepared solution. Here, the working electrode was the microfluidic channel. The channel had a coating of chrome (35 nm) and gold (65 nm) over Parylene C coating to provide a conductive surface. The electrosynthesis was done using the cyclic voltammetry (CV) method (-0.2 to 0.8 V, 6 cycles at a scan rate of 50 mV/s) by VersaSTAT 4 Potentiostat Galvanostat, and the MIP thin film (polypyrrole) covered the working electrode at the end the electrosynthesis. The template molecule was trapped in this synthesized polymer. The extraction step was taken by immersing the working

electrode in an extraction solution (methanol and acetic acid mixture with a ratio of 9:1) and keeping it there for about 2 hours while shaking slowly. It left behind particular cavities created especially for the template (THC). Scanning electron microscopy (SEM) and X-ray photoelectron spectroscopy (XPS) were used to characterize and study the microchannels before and after coating. When the template is absent during synthesis, a control known as a non-imprinted polymer (NIP) is produced. For NIP thin film, no template (THC) was added to the solution, and no extraction and washing was needed. All other steps were the same as MIP thin film. A channel before and after MIP thin film coating can be seen in Figure 2.

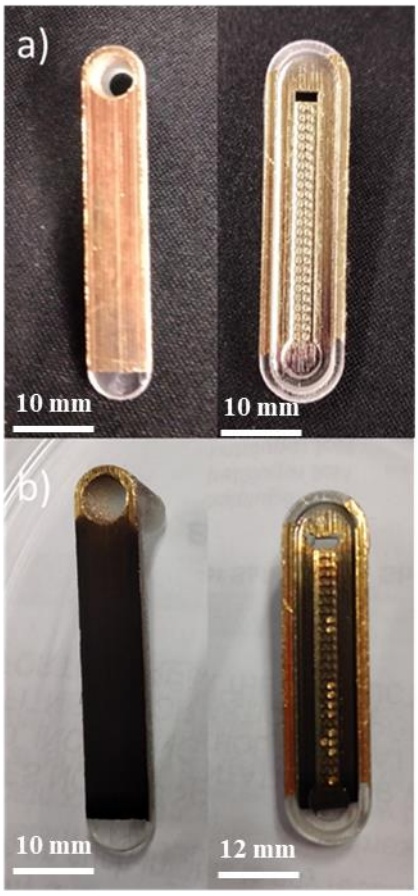

Figure 2 - Microchannel a) before and b) after MIP thin film coating

2.3 MIP NPs synthesis

The MIP and NIP NPs were synthesized using the precipitation procedure. For MIP NPs, methacrylic acid (3 mmol) and THC (1 mmol) were added to 30 ml acetonitrile, and the incubation of the mixture took about 20 minutes. After adding AIBN (80 mg) and EGDMA (3mmol) to the mixture, Nitrogen was used to purge it for about 15 minutes. The mixture was put in a sealed glass bottle. An oil bath at the temperature of 60–65 °C was used for the polymerization. It occurred thermally by keeping the bottle in the oil bath for 15 h while the mixture was stirred. In Figure 3, the thermal polymerization in an oil bath and the product can be seen. For NIP NPs, THC was eliminated from the ingredients, and the same steps were taken. Following polymerization, the solution was centrifuged, and the resulting polymer was ground into a powder. The following step is only for MIP powder to remove the template. It was washed with acetonitrile after putting it in the sonic bath for about 10 minutes and stirring it for 10 minutes. SEM and Raman spectroscopy were used to characterize and study the morphology and chemical structure of NPs.

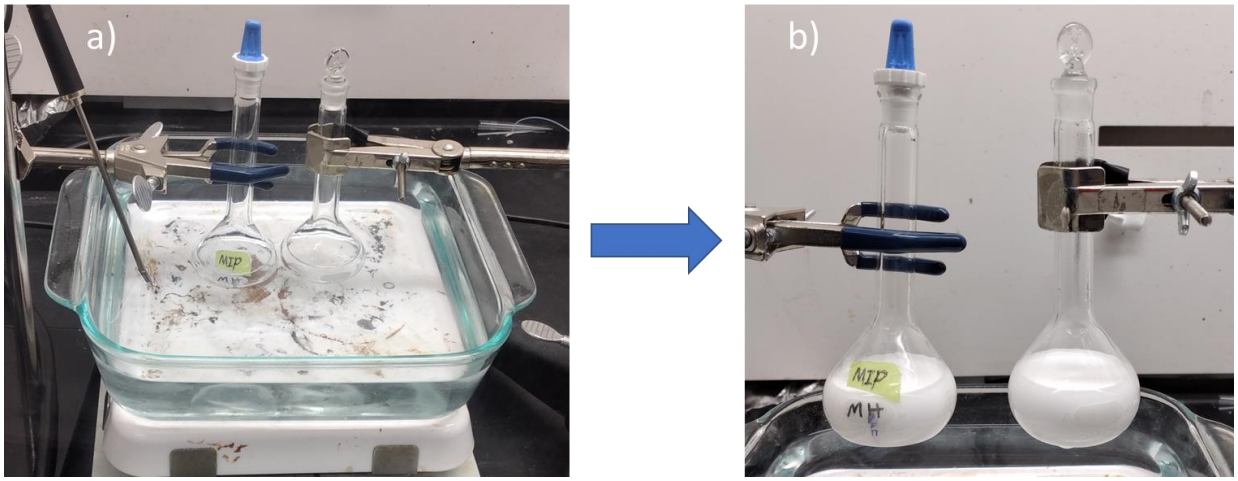

Figure 3 - a) Polymerization in oil bath. b) Product.

2.4 MIP and NIP thin film coated channels

The MIP and NIP thin films were coated on the MIP and NIP channels, respectively, using the electropolymerization technique. The microfluidic channel acted as the working electrode in the three-electrode experimental setup, and the polymerization occurred on its surface. The polymerization was followed by the washing step for the MIP channel to extract the template. To do so, the coated channel was kept in a tube filled with methanol and acetic acid with a ratio of 9:1. The process took about 2 hours, during which the tube was shaken on a shaker. After this step, the channel was kept in the fume hood to dry. Then, two parts of the channel were put together, and the MOS sensor was placed at the end of the channel on its predetermined sitting. No washing was needed for the NIP channel, and the rest of the process was the same. This channel was coated with NIP thin film, which had no recognition sites in its structure, and it was the only difference between this channel and the three MIP channels coated with MIP thin film. This channel worked as the control channel to be compared with the MIP channels to see the effect of binding sites for THC, which exist in the MIP thin film structure. There were three MIP channels, and the only difference between these channels was in the monomer (pyrrole): template (THC) ratio of MIP thin film coated on the channel. The monomer (pyrrole): template (THC) ratio of MIP thin film is an influential parameter in the performance of the channel since it impacts the formation of recognition sites in the MIP thin film structure. So the level and strength of the interaction between binding sites and analytes, especially THC, is influenced by this ratio. All the above mentioned four channels were exposed to 300, 400, 500, 600, and 700 ppm of THC, CBD, methanol, and ethanol. The performance of these MIP channels was compared to each other to find the best channel and ratio among them. To do so, the performance parameters for each MIP channel were calculated and compared to the values gained for the NIP channel.

2.5 MIP and NIP NPs coated channels

The MIP and NIP NPs were coated on the MIP and NIP channels, respectively, after oxygen-plasma-treating of Parylene C-coated microchannels. Specific recognition sites for THC are present in the MIP NPs channel, while the NIP NPs channel has no recognition sites in its structure and acts as the control channel. The coating on the channels was done by the drop-casting method. The MOS sensor is then positioned at the end of the channel on its specified sitting after the two channel pieces have been assembled. The MIP and NIP channel were exposed to 300, 400, 500, 600, and 700 ppm of THC, CBD, methanol, and ethanol. The performance parameters for the MIP and NIP NPs channels were calculated and compared to each other to find the effect of recognition sites in the MIP NPs structure.

2.6 Microchannel and NPs Characterization

To study the size, shape, layout, and chemistry of the synthesized NPs and the microchannel surface before and after the coating, scanning electron microscopy (SEM), Raman spectroscopy, and X-ray photoelectron spectroscopy (XPS) were conducted.

2.6.1 Scanning electron microscopy (SEM)

SEM is a particular kind of microscope that scans a focused electron beam to produce enlarged pictures of a target item [90]. A vacuum is created in the microscope chamber by specific pumps, and the target sample is put inside the chamber. The vacuum level within the chamber is determined by the microscope's design. While some microscopes function best in low vacuum conditions, some perform well in high vacuum conditions [91]. An electron cannon is used to emit electrons, which go through a series of lenses and form a focused beam that interacts with the surface of the target material. Different signals, including secondary electrons, backscattered electrons, and distinctive X-rays, are created when the target material and the electron beam

interact. The generated signals are detected by various detectors, which then yield the pictures [92], [93].

2.6.2 X-ray Photoelectron Spectroscopy (XPS)

A method for examining a material's surface chemistry is XPS. This technique allows for the identification and measurement of the elements, chemical states, electronic states, and bound elements present in the target material [94], [95]. The target sample's surface is exposed to an X-ray beam, and special detectors are used to calculate the kinetic energy of the electrons that are emitted. By observing ejected electrons at various kinetic energies, a spectrum is created. The energy and intensities of the spectrum peaks aid in the identification and measurement of surface elements since different atoms emit electrons with various characteristic energies [96].

2.6.3 Raman spectroscopy

The molecules in a target sample may be identified using Raman spectroscopy characterization tests. This arrangement is a subfield of vibrational spectroscopy in which a sample is subjected to a laser or other strong light beam. After the creation of a scattered photon, the frequency shift of inelastically scattered light from the sample is measured [97]–[101]. The components of a Raman spectrometer include a light source, a monochromator, a sample holder, and a detector [102].

2.7 Response Analysis

Sensor relative response, sensitivity, selectivity, and recovery time are a few examples of the metrics that can be used to evaluate the performance of microfluidic gas sensors. The relative response ($\Delta R/R_a\%$) is defined as $\Delta R/R_a\% = \frac{R_a - R_g}{R_a} \times 100$, where R_a is sensor resistance in clean air, and R_g is sensor resistance when it was exposed to gas [103], [104].

The slope of the sensor's relative response versus the analyte concentration (i.e., the calibration curve) is the definition of sensitivity. The calibration curves and sensitivity indicators were obtained using five different concentrations of the target analytes (300, 400, 500, 600, and 700 ppm of THC, CBD, Methanol, and Ethanol).

A gas sensor's selectivity demonstrates how well it can distinguish between response signals from various analytes. In this work, two features were extracted from each response signal using the Principal Component Analysis (PCA) method (Using MATLAB R2021b) to quantitatively analyze and show the sensors' selectivity. In a 2D feature space, these features can be utilized to visually illustrate the selectivity. To compare the separation ability and selectivity of different sensors toward THC quantitatively, the 2D Euclidean distance between the average of THC's PCs distribution and that of another analyte for each sensor, $Sel = \sqrt{(Avg\ (PC1_{THC}) - Avg\ (PC1_i))^2 + (Avg\ (PC2_{THC}) - Avg\ (PC2_i))^2}$, was used [70], [105]. In the abovementioned equation, *Sel* is the selectivity indicator, $PC1_{THC}$ and $PC1_i$ are principal component 1 values for THC and target analyte i, respectively, and $PC2_{THC}$ and $PC2_i$ are principal component 2 values for THC and target analyte i, respectively.

Recovery time is the required time for the signal to return to baseline value after stopping the exposure, and here it is defined as the time required for the signal to increase by 90% of the difference between maximum and minimum values of the signal [106].

2.8 Principal Component Analysis (PCA)

One of the most often used techniques for dimension reduction and multivariate analysis in the literature is PCA [107]. It is a method of distance-based ordination designed to find patterns in large datasets. By signaling new and reduced features in lower dimensions, PCA attempts to preserve all significant information from the data by creating new spanning vectors. The method's

main goal is to identify and describe the underlying pattern in order to determine the connection between variables [108].

2.9 Test setup and data capturing

A static system allowing the generation of different vapor concentrations was used to study the performance of the channels toward different analytes. A precise micro sampler was used to inject each VOC (methanol and ethanol) separately into a 40-liter chamber through an analyte injection valve on top of the chamber. Then it was left to evaporate. For THC and CBD, a heater is needed to evaporate them. So they were put on a heater (5 V ceramic heating plate) placed in the chamber for this purpose. To ensure the uniform distribution and circulation of analyte vapor in the chamber, a mini fan (5 V LD3007MS mini fan) was placed in the chamber, and the exposure began about 15 mins after the addition of the analyte to the chamber. The channels were simultaneously exposed to the chamber vapor and then let to recover in clean air. The simultaneous exposure and exact timing were provided by a board and a linear actuator. It is important because it helps to eliminate any undesirable effects, such as alterations in the analyte's concentration in the chamber. To do so, the channels were placed on the board, which was connected to the linear actuator controlled by a raspberry pi. By controlling the linear actuator and the board, the holes on the chamber face the inlet of the channels for exposure or are blocked to prevent exposure. The responses toward 300, 400, 500, 600, and 700 ppm of each analyte were obtained. A raspberry pi microcontroller and the manufacturer's electronic circuit were used to record signals. All the tests were done in the fume hood, and before each test, the chamber was purged with clean air. Data capturing for each test was done in three stages; 1) In clean air without the analyte to check the baseline and recovery from the previous test, 2) during the exposure to the analyte, and 3) after stopping the exposure and during the recovery step in the clean air. This process was repeated four

times for each test to ensure the repeatability of the test. A temperature sensor and a humidity sensor were in the chamber, and all tests were conducted at the same temperature and humidity. The experimental setup can be seen in Figure 4.

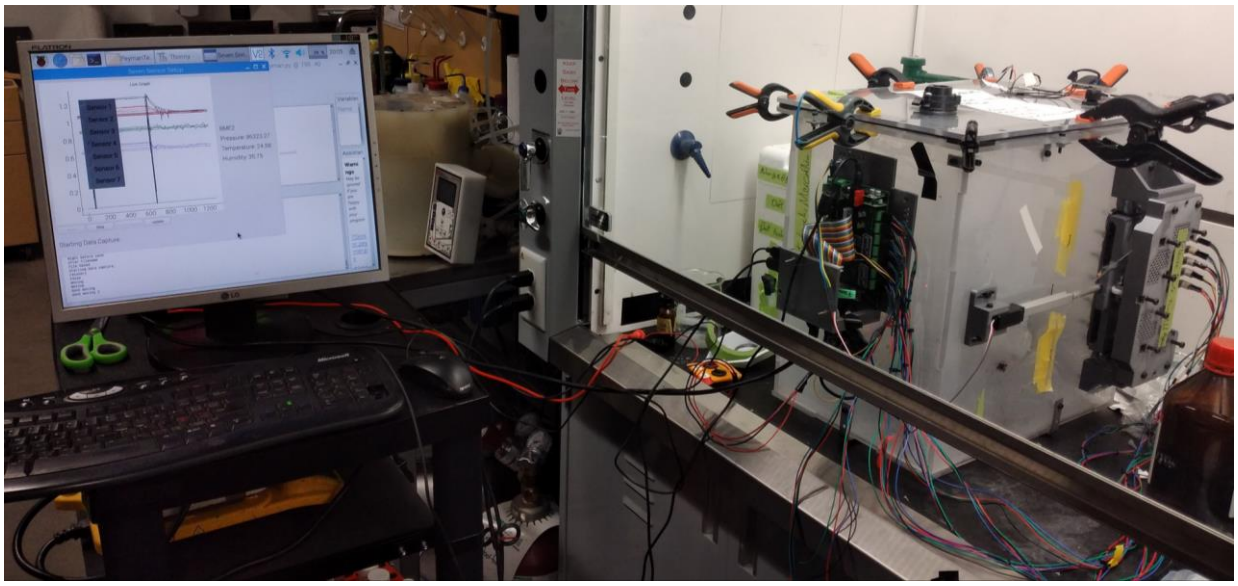

Figure 4 - Experimental setup for gas sensing tests and data capturing

Chapter 3: Results and discussion

3.1 Characterization results

3.1.1 MIP and NIP NPs SEM

The SEM image and size distribution of MIP NPs can be found in Figure 5. SEM imaging demonstrated spherical MIP NPs morphology with an average size of 168±19 nm. The measurement was done on 100 particles with the standard deviation of 19 nm and coefficient of variation (CV) of 11.31% which is a very good and acceptable CV%.

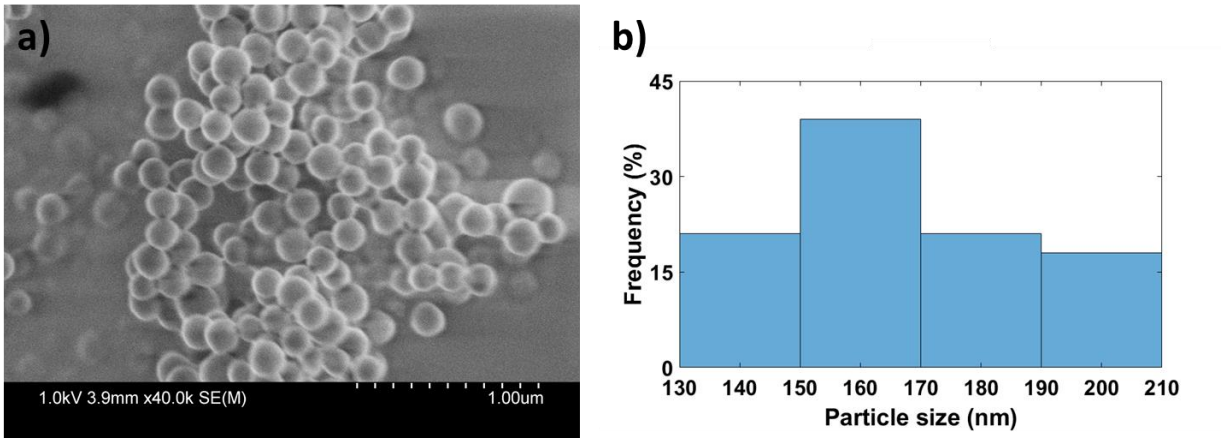

Figure 5 – a) SEM image and b) size distribution of MIP NPs

Figure 6 shows the SEM image and size distribution of NIP NPs. Spherical NIP NPs morphology with an average size of 753±75 nm can be found in this figure. 100 particles sizes were measured and the standard deviation was 75 nm and the coefficient of variation (CV) was 10% which is a very good and acceptable CV%.

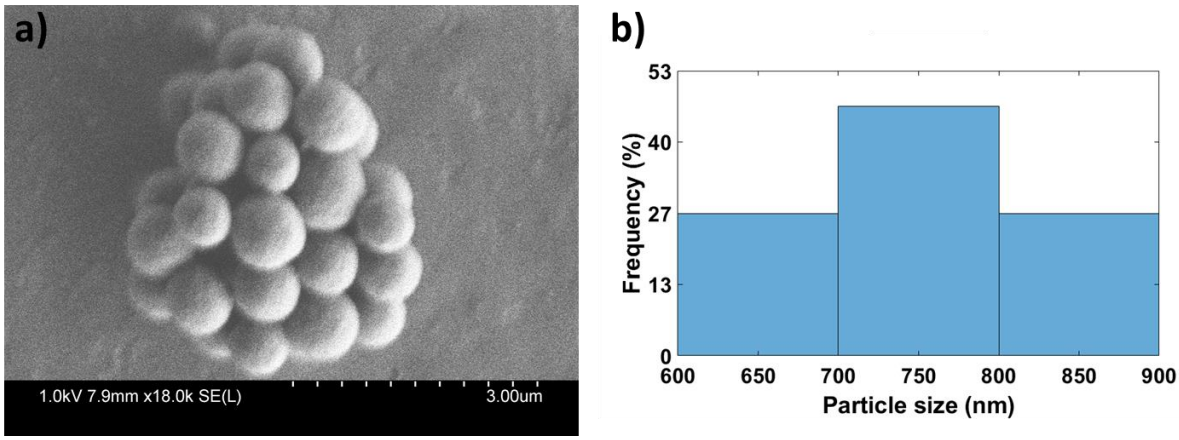

Figure 6 - a) SEM image and b) size distribution of NIP NPs

The uniformity in shape and size distribution is attributed to the advantage of precipitation polymerization method.

3.1.2 MIP and NIP NPs Raman Spectroscopy

Here we use Raman spectroscopy for the detection of small volumes of target molecules of THC in MIP samples on a solid surface as well as verifying the molecular imprinting of the polymers. The Raman spectra of imprinted MIP (MIP before template extraction), extracted MIP (MIP after template extraction),and NIP are shown in Figure 7. As expected, the imprinted MIP Raman spectrum is totally different from extracted MIP and NIP spectra, while there is no remarkable difference between extracted MIP and NIP spectra. Distinguishable peaks in 1300, 1450, 1600, and 2950 cm^{-1} regions of imprinted MIP spectrum decreased dramatically in extracted MIP spectrum, resulting in an almost identical spectrum to the NIP spectrum. Also, in 2950 cm^{-1} region a shift in the wavenumber of peak can be seen in the imprinted MIP spectrum compared to the NIP and the extracted MIP spectra. These difference are attributed to the presence of THC in imprinted MIP and its absence in extracted MIP and NIP.

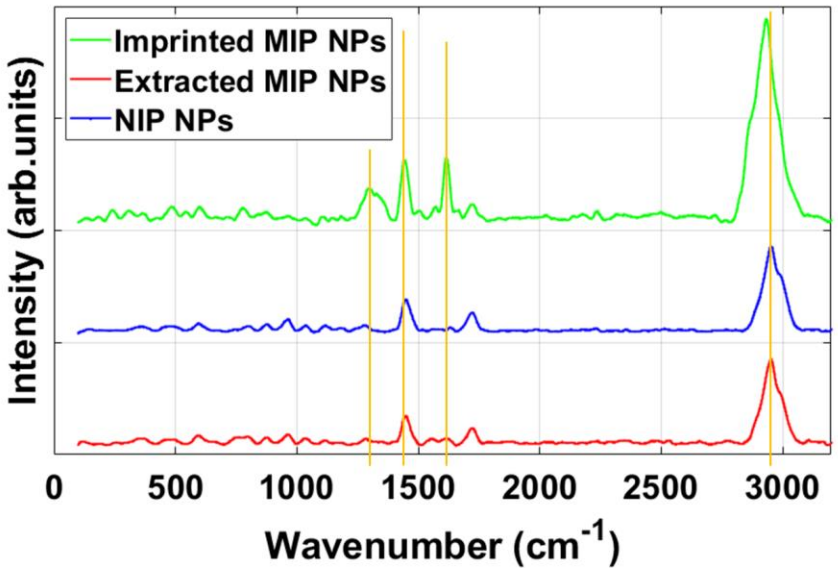

Figure 7 - Raman spectra of imprinted MIP NPs, extracted MIP NPs, and NIP NPs

3.1.3 MIP and NIP thin film coated microchannels SEM

Figure 8 presents the SEM images of the channel surface before and after MIP coating. The SEM images confirmed the successful modification of the surface with the MIP thin film. As shown, the surface morphology of the channel was changed after MIP thin film coating. It can be clearly seen that the MIP film uniformly distributed with ripples on the surface. The formation of ripples and the thickness are attributed to the viscosity and concentration of the MIP.

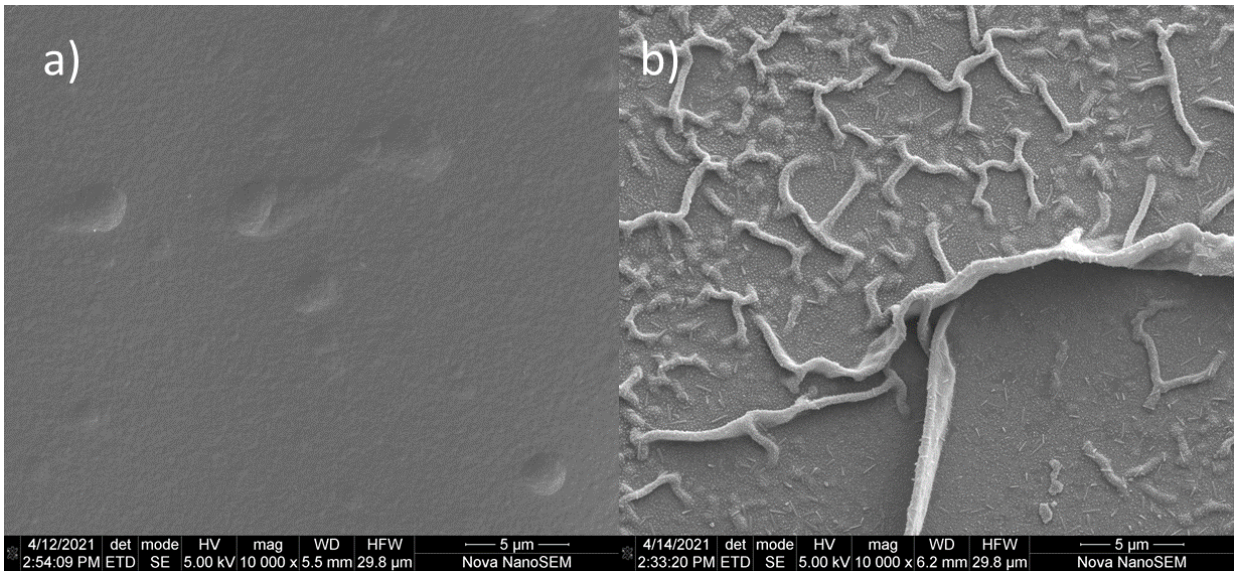

Figure 8 - SEM images of surface a) before and b) after MIP thin film coating

3.1.4 MIP and NIP thin film coated microchannels XPS

XPS spectra used to provide the information concerning the chemical composition of a 3d printed surface, Parylene c, gold, and MIP thin film-coated surfaces (Figure 9). Comparing the spectrum before and after Parylene C coating, an increase can be seen in Cl 2p peak attributed to chemical composition of Parylene C. After coating of gold, the Au peaks were clearly increased in intensity, and peaks related to Cl 2p and C 1s decreased. Carbon and Nitrogen are two elements of MIP (polypyrrole) and can be seen in high intensity as C 1s and N 1s peaks after coating of MIP thin film on gold. Table 1 shows the information about the surface chemical composition at different coating steps.

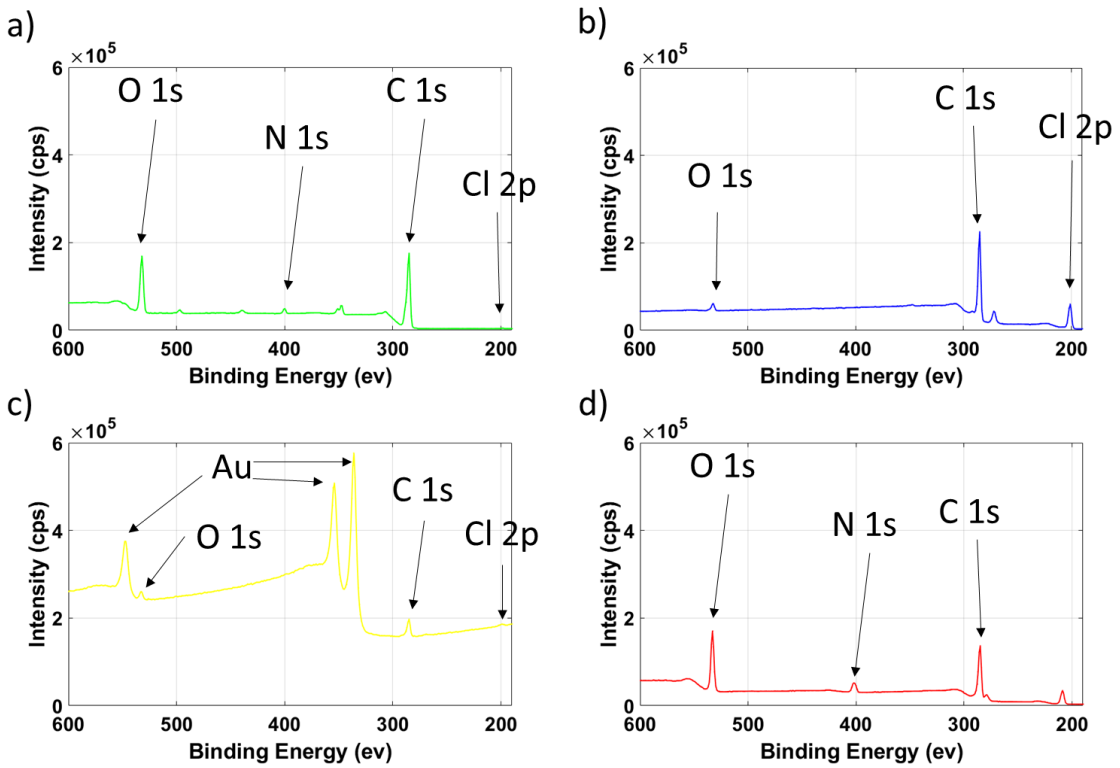

Figure 9 - XPS results of a) 3dprinted surface b) Parylene C coated surface c) Gold coated surface, and d) MIP thin film coated surface

Table 1 - XPS results including peaks and row area

3dprinted		PC	
Peak	Row Area (cps ev)	Peak	Row Area (cps ev)
C 1s	628365.8	C 1s	636144.2
O 1s	468946.7	O 1s	63003.3
N 1s	34650.8	Cl 2p	197900
Cl 2p	1483.3		
Gold		MIP	
Peak	Row Area (cps ev)	Peak	Row Area (cps ev)
C 1s	150469.2	C 1s	405643.3
O 1s	58330	O 1s	466484.2
Cl 2p	22460	N 1s	97643.3

3.2 Gas sensing results

The performances of the microfluidic gas sensors were investigated based on their response to gas exposure.

3.2.1 MIP and NIP NPs coated channels

Figure 10 a) and Figure 11 a) display the responses of NIP and MIP NPs channels, respectively, to 600 ppm of different analytes (THC, CBD, methanol, ethanol). As expected, there is a huge difference between the THC response curve for the MIP channel and the NIP channel (the minimum resistance value and recovery time). The amount of drop in the resistance value for the MIP channel is much lower than that of the NIP channel showing the trapping of THC molecules in the cavities. The longer recovery time is a good indicator of strong molecule-binding site interaction. The difference in MIP and NIP channel responses toward each of the other analytes (CBD, methanol, ethanol) shows the interaction of recognition sites with each of them, but it is obvious that these interactions are much less and weaker than that of THC. Among tested analytes, CBD has the most similar structure to THC, and the response of the MIP channel sensor toward CBD shows it. Compared to methanol and ethanol, its minimum resistance is closer to THC, which shows more interaction with cavities. The longer recovery time, compared to methanol and ethanol, shows a stronger interaction between CBD molecules and binding sites. As can be seen in the MIP channel responses, among different analytes, methanol's and ethanol's NIP channel responses are better maintained. They are too small to interact with the recognition sites of THC, and if there is any interaction, it will be so weak. Therefore, no huge difference is expected between MIP and NIP channel responses for methanol and ethanol.

Figure 10 b) and Figure 11 b) show the resistance-time curves of NIP and MIP NPs channels to 600 ppm of THC, respectively, during four consecutive cycles indicating full recovery after each round and repeatability of the test.

The calibration curve (relative response versus concentration curve) of NIP and MIP NPs channels can be seen in Figure 10 c) and Figure 11 c), respectively. The effect of concentration change of an analyte on the response is visualized for both MIP and NIP channels. There are three clusters in the MIP curve. The first is the THC cluster. The second one is CBD. The third one includes methanol and ethanol. There are no distinguishable and meaningful clusters in the NIP curve. These observations were expected based on the provided discussion on the results. As it was mentioned, the test for a specific concentration of a specific analyte repeated four times. After calculation of the mean, standard deviation, and coefficient of variation (CV) for relative response of four replications of each test, the maximum CV was about 5% which is very good and acceptable.

The calculated PC1 and PC2 for each test response have been visualized in Figure 10 d) and Figure 11 d) for the NIP and MIP NPs channels, respectively. Each point displays the PC1 and PC2 for the response of the channel toward a determined concentration of a determined analyte. Unlike the NIP channel, the MIP channel successfully separated THC from other analytes demonstrating its selectivity toward THC because of MIP NPs' recognition sites for THC. The quantitative selectivity indicator toward THC is calculated as the 2D Euclidean distance between the average values of PC1 and PC2 for THC distribution and that of other analytes' distributions. By sorting these values from the largest to the smallest, we will have (THC-ethanol> THC-methanol)>> THC-CBD. The larger amount of distance means a bigger difference and more selectivity between those two analytes. Among the analytes, CBD has the most similar structure

to THC and more interaction with the binding sites, so their distance from each other is the smallest. Methanol and ethanol are too small for the cavities and have the least interaction with them, so they have greater distance from THC.

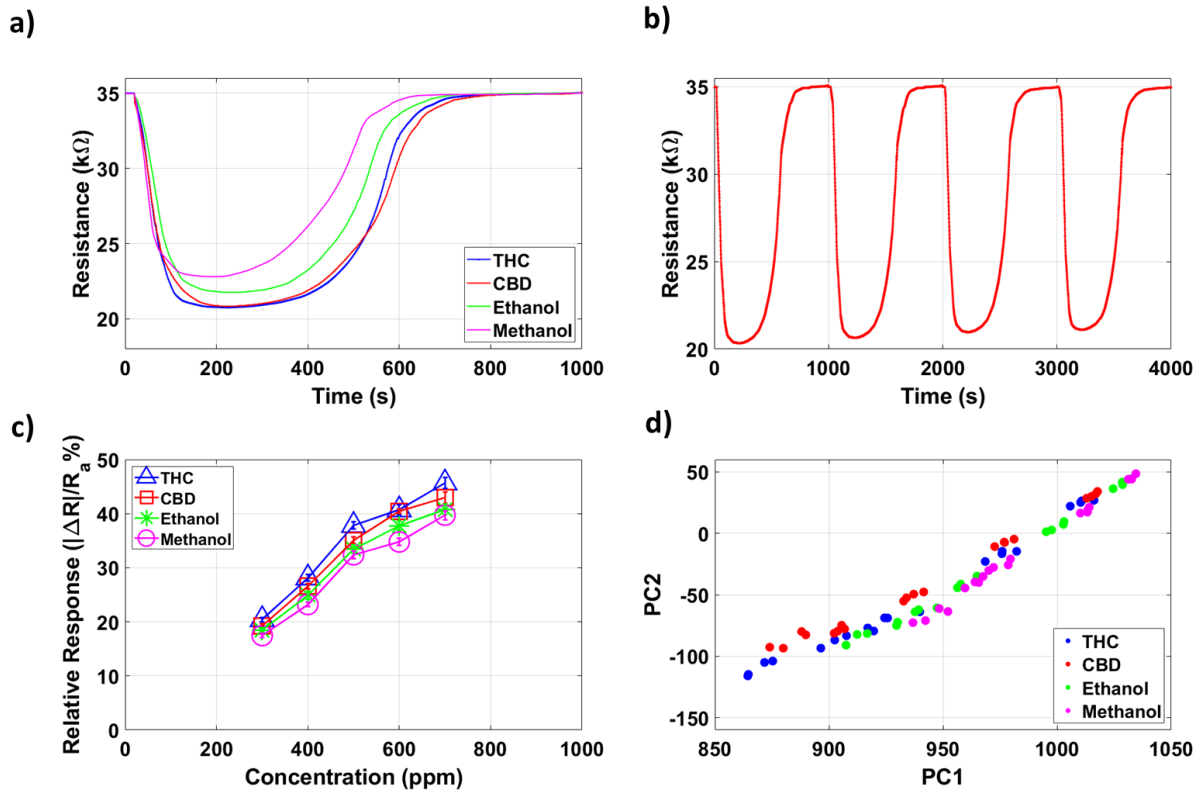

Figure 10 - a) NIP NPs channel's MOS sensor resistance change upon exposure to 600 ppm of four different analytes. b) NIP NPs channel's MOS sensor resistance change for four consecutive cycles of exposure to 600 ppm of THC. C) The calibration curve (the sensor relative response versus the concentration of the analyte) for NIP NPs channel exposed to four analytes. d) The PC1 and PC2 presentation of different analytes for NIP NPs channel.

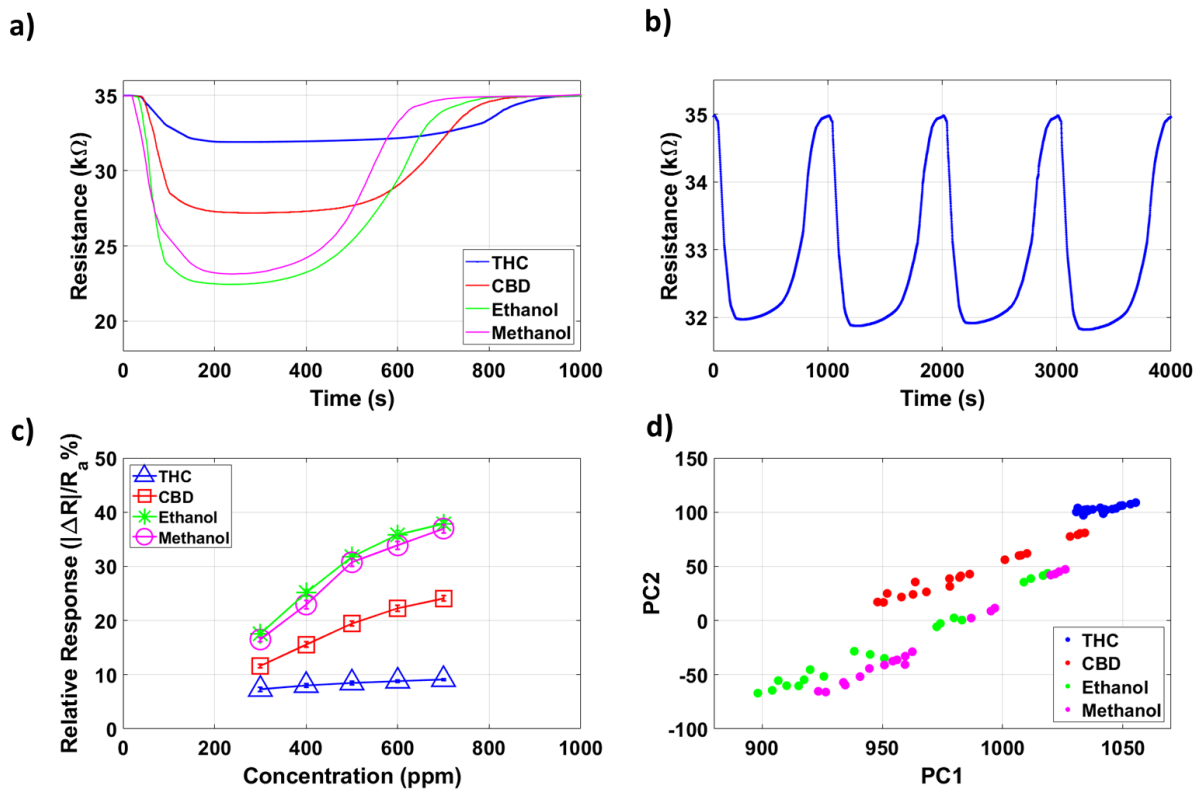

Figure 11 - a) MIP NPs channel's MOS sensor resistance change upon exposure to 600 ppm of four different analytes. b) MIP NPs channel's MOS sensor resistance change for four consecutive cycles of exposure to 600 ppm of THC. C) The calibration curve (the sensor relative response versus the concentration of the analyte) for MIP NPs channel exposed to four analytes. d) The PC1 and PC2 presentation of different analytes for MIP NPs channel.

The response of MIP and NIP channels to different concentrations (300 to 700 ppm) of THC, CBD, ethanol, and methanol can be seen in Figure 12 a), b), c), and d), respectively. The NIP channel response curves for different analytes have a roughly similar shape with slightly different minimum values. However, the MIP channel response curve for THC is totally different from that of other analytes due to the specific interaction of cavities with THC, which improves the selectivity toward THC. No partial recovery was observed. For both channels, exposure to higher concentrations of the analyte results in an increase in the amount of resistance drop. Due to

the presence of cavities in the MIP channel and desirable or undesirable interaction of them with analytes, the amount of it for the MIP channel is smaller than that of the NIP channel for all analytes. Among different analytes' MIP channel responses, THC response show the least change resulted from concentration alteration indicating the best and strongest MIP NPs-analyte interaction. Methanol and ethanol response show the most change indicating the weakest MIP NPs-analyte interaction.

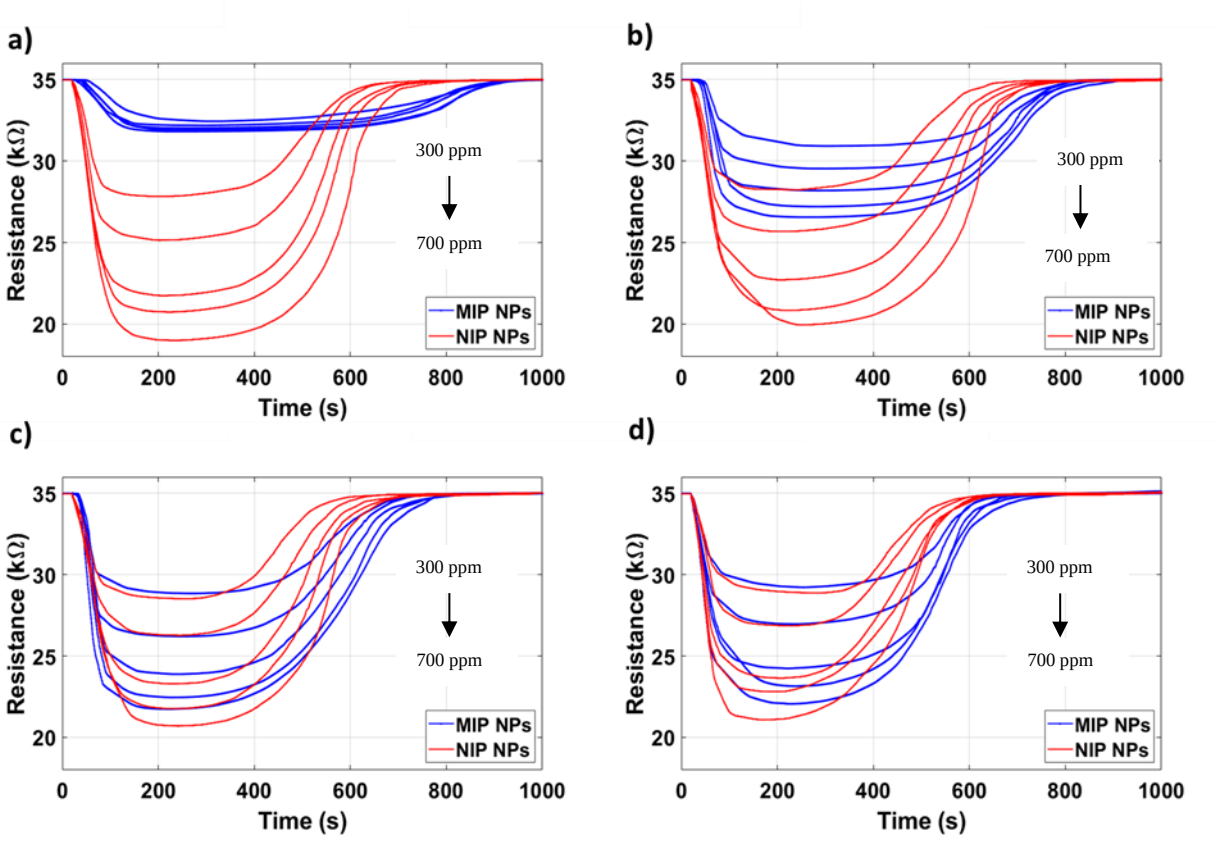

Figure 12 – The resistance versus time graphs for two channels upon exposure to five different concentrations (300 ppm–700 ppm) of a) THC, b) CBD, c) ethanol, d) methanol.

No specific recognition sites exist in the structure of NIP NPs, and no remarkable difference is observed between the responses toward different analytes. For example, for 500 ppm of methanol, ethanol, CBD, and THC, the relative responses were 32.39%, 33.42%, 35.07%, and

37.83%, respectively, and the recovery time for that were 238 s, 266 s, 321 s, and 299 s, respectively. The selectivity toward THC was quantified by calculating the 2D Euclidean distance. For 500 ppm, the distance between THC and CBD were found to be 20.78.

Compared to NIP NPs, considering the MIP NPs' response toward 500 ppm of methanol, ethanol, and CBD, the relative responses were 30.75% (5% decrease), 31.77% (5% decrease), and 19.43% (45% decrease), respectively, and recovery times were 290 s (18% increase), 353 s (25% increase), and 453 s (29% increase), respectively. While for 500 ppm of THC, there was a decrease of 78% in relative response (8.48%) and an increase of about 46% in the recovery time (555 s). The channel's sensitivity toward THC had 93% decrease, while it was 17% decrease for methanol and ethanol and 33% decrease for CBD. For 500 ppm, the 2D distance between THC and CBD were 84.01 (304% increase). This channel is more selective to THC than NIP NPs channel.

3.2.2 MIP and NIP thin film coated channels

Figure 13 a), Figure 14 a), Figure 15 a), and Figure 16 a) show the responses of NIP thin film, MIP thin film 1, 2, and 3 channels, respectively, to 300 ppm of different analytes (THC, CBD, methanol, ethanol). The MIP channels' responses to THC were different from the NIP channel's, which is to be anticipated. The resistance value dropped in all channels, but the MIP channels' decline was less than the NIP channel's drop indicating that THC molecules were trapped in the cavities. It is clear that the interaction of recognition sites with the other analytes (CBD, methanol, ethanol) is less and weaker than that of THC, as shown by the differences in MIP channels and NIP channel responses toward each of them.

The resistance-time curves of NIP thin film, MIP thin film 1, 2, and 3 channels to 300 ppm of THC over the course of four consecutive tests are shown in Figure 13 b), Figure 14 b), Figure

15 b), and Figure 16 b), respectively, demonstrating complete recovery after each round and repeatability of the test.

The relative response-concentration curve, the calibration curve, of NIP thin film, MIP thin film 1, 2, and 3 channels have been presented in Figure 13 c), Figure 14 c), Figure 15 c), and Figure 16 c), respectively. Among the MIP thin film channels, MIP thin film 1 has the greatest monomer (pyrrole): template (THC) ratio resulting in self-aggregation and an increase in the nonselective interaction of binding sites with analytes other than THC. MIP thin film 3 has the lowest monomer (pyrrole): template (THC) ratio resulting in less than ideal assembly and the lack of appropriate binding sites. The results obtained from these channels support the provided discussion. By comparing NIP channel response to CBD, ethanol, and methanol with MIP thin film channels, it can be observed that the relative response decrease for MIP thin film 1 is greater than that of MIP thin film 2 and 3, indicating the nonselective interaction with CBD, ethanol, and methanol. Also, by comparing NIP channel response to THC with MIP thin film channels, it is evident that the lowest decrease is for MIP thin film 3, indicating the lack of binding sites and assembly. We can see how varying analyte concentrations affect the resulting response. The MIP thin film 2 curve can be divided into three distinct groups. The THC cluster comes first. CBD is the second. Methanol and ethanol are components of the third. The NIP thin film, does not break down into relevant subgroups. The mentioned clusters are not clearly distinguishable in MIP thin film 1, and MIP thin film 3 curves. Each concentration of each analyte was tested four times. The greatest coefficient of variation (CV) for relative response of four replications of each test was 8% which is satisfactory and acceptable.

After extracting the two first principal components (PC1 and PC2) from each response, a 2D plot presented them. Figure 13 d), Figure 14 d), Figure 15 d), and Figure 16 d), show them for

NIP thin film, MIP thin film 1, 2, and 3 channels, respectively. A channel's PC1 and PC2 for its response to a determined concentration of an analyte are shown for each data point. In this case and by observing these four graphs, it can be said that the more compact the THC cluster, the more selective the channel is.

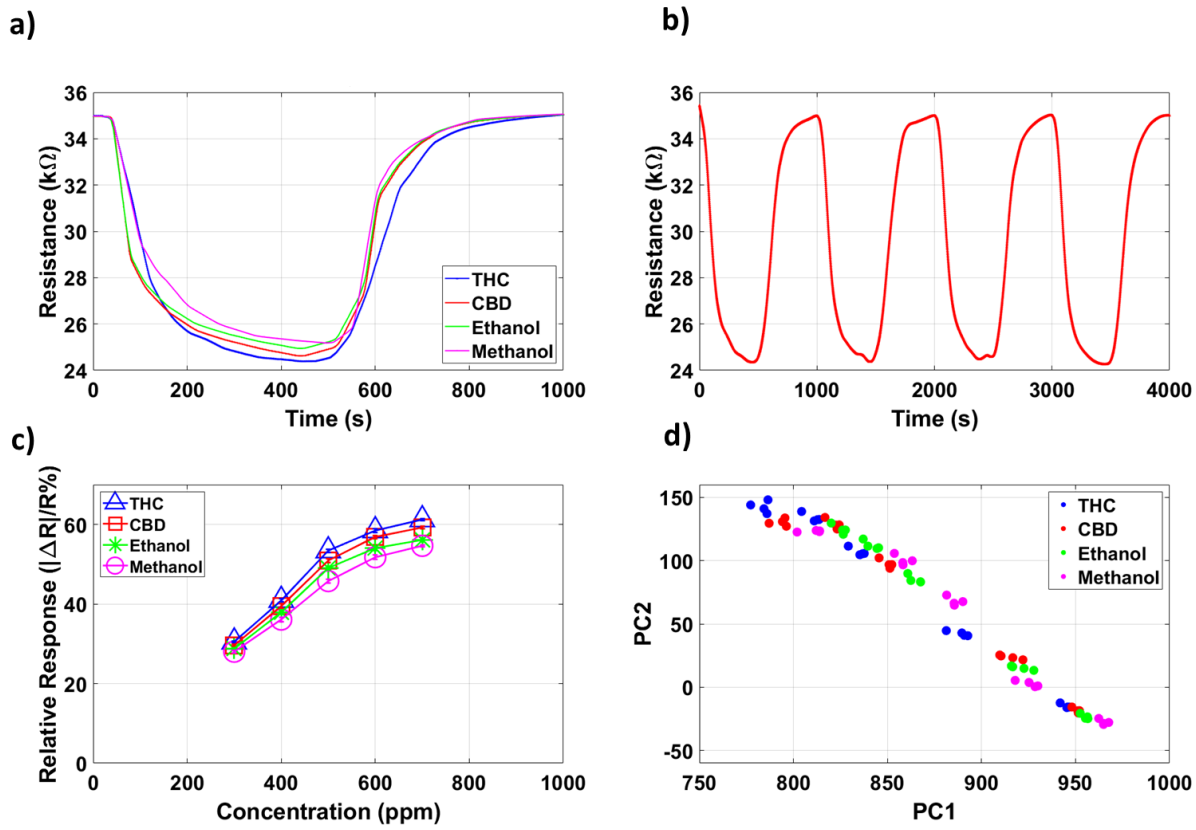

Figure 13 - a) NIP thin film channel's MOS sensor resistance change upon exposure to 300 ppm of four different analytes. b) NIP thin film channel's MOS sensor resistance change for four consecutive cycles of exposure to 300 ppm of THC. C) The calibration curve (the sensor relative response versus the concentration of the analyte) for NIP thin film channel exposed to four analytes. d) The PC1 and PC2 presentation of different analytes for NIP thin film channel.

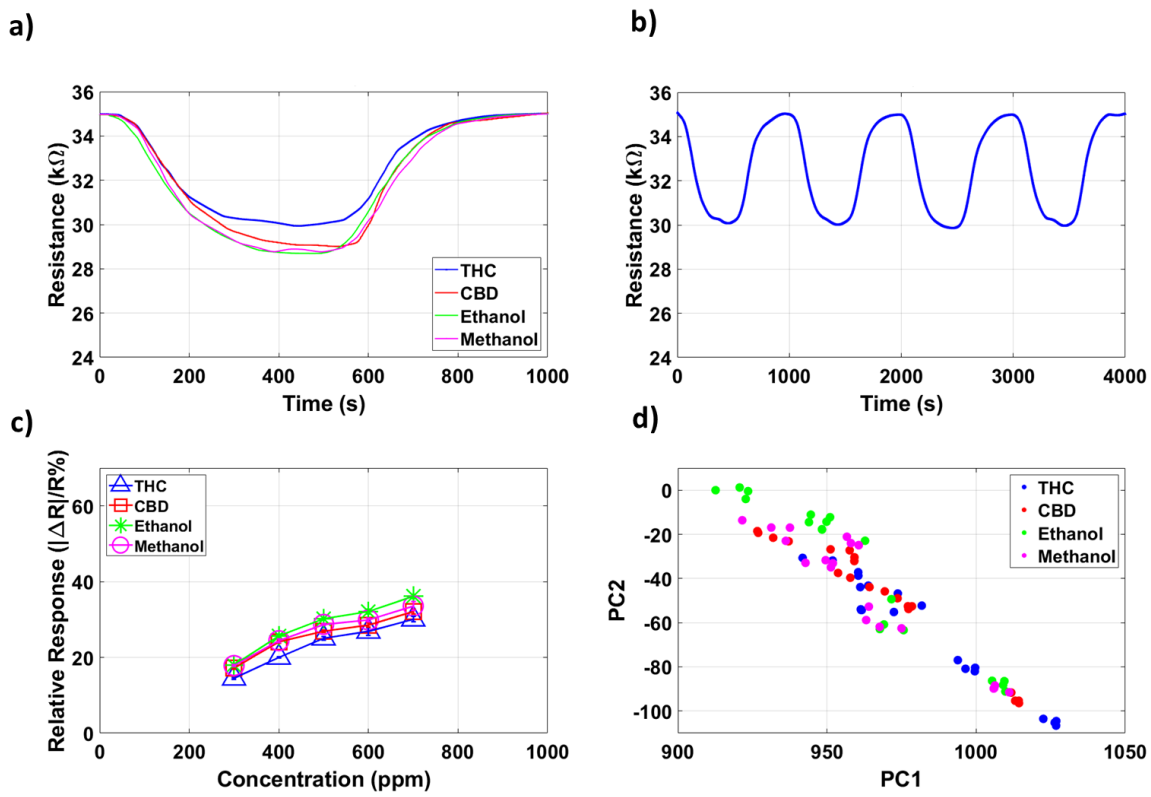

Figure 14 - a) MIP thin film 1 channel's MOS sensor resistance change upon exposure to 300 ppm of four different analytes. b) MIP thin film 1 channel's MOS sensor resistance change for four consecutive cycles of exposure to 300 ppm of THC. C) The calibration curve (the sensor relative response versus the concentration of the analyte) for MIP thin film 1 channel exposed to four analytes. d) The PC1 and PC2 presentation of different analytes for MIP thin film 1 channel.

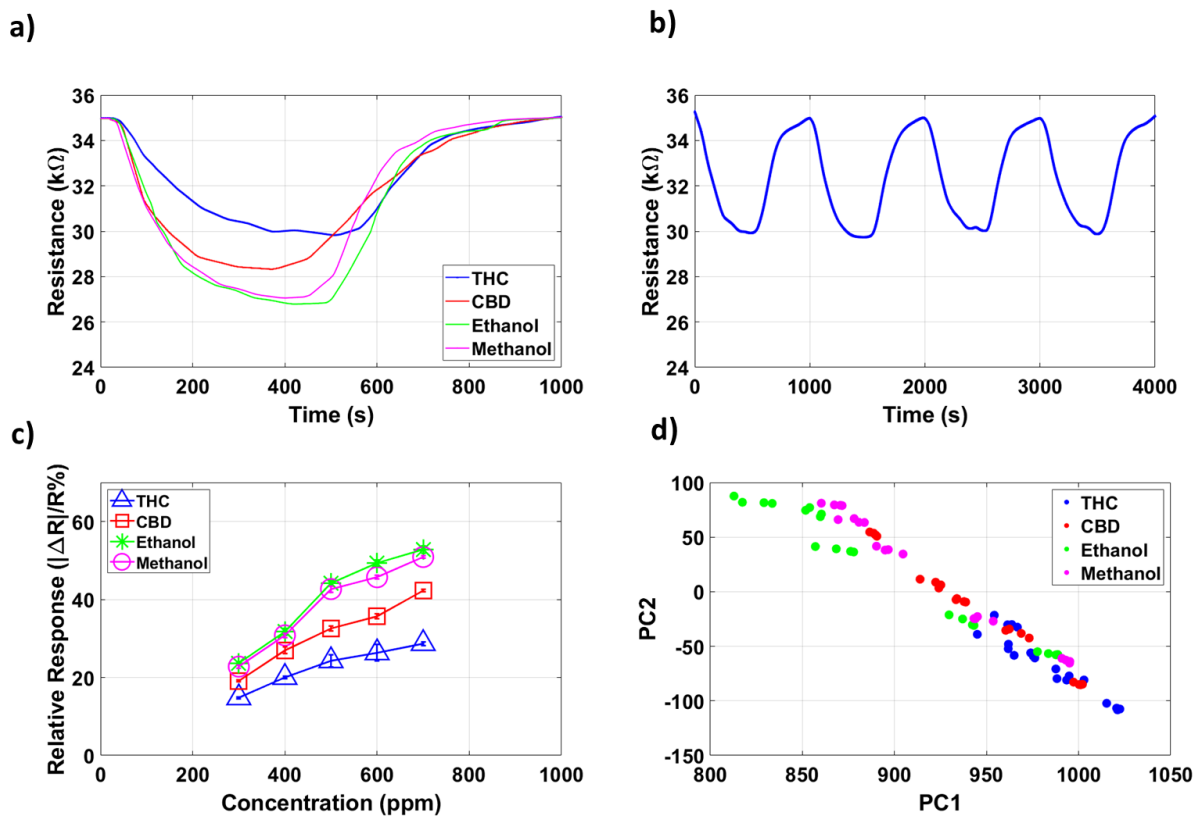

Figure 15 - a) MIP thin film 2 channel's MOS sensor resistance change upon exposure to 300 ppm of four different analytes. b) MIP thin film 2 channel's MOS sensor resistance change for four consecutive cycles of exposure to 300 ppm of THC. C) The calibration curve (the sensor relative response versus the concentration of the analyte) for MIP thin film 2 channel exposed to four analytes. d) The PC1 and PC2 presentation of different analytes for MIP thin film 2 channel.

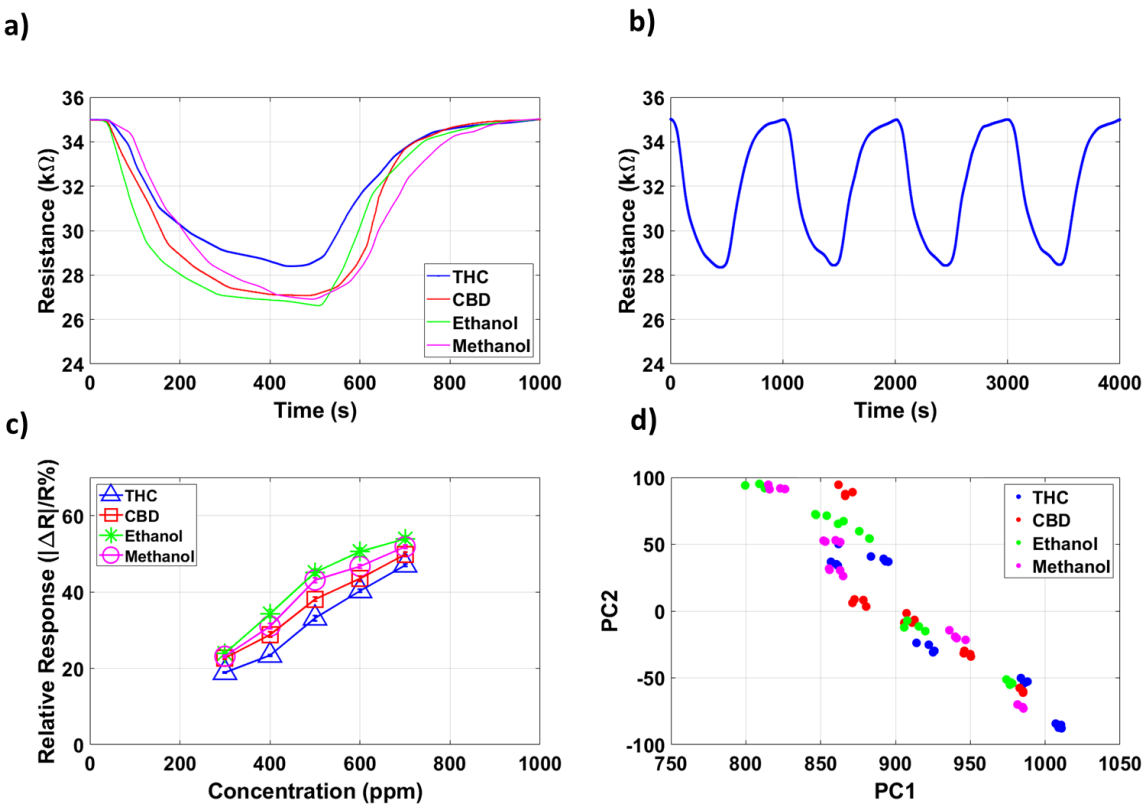

Figure 16 - a) MIP thin film 3 channel's MOS sensor resistance change upon exposure to 300 ppm of four different analytes. b) MIP thin film 3 channel's MOS sensor resistance change for four consecutive cycles of exposure to 300 ppm of THC. C) The calibration curve (the sensor relative response versus the concentration of the analyte) for MIP thin film 3 channel exposed to four analytes. d) The PC1 and PC2 presentation of different analytes for MIP thin film 3 channel.

No considerable difference is seen in the response of NIP thin film channel to the same concentration of different analytes. The amount of resistance drop because of exposure to an equal concentration of different analytes is approximately the same. The selectivity indicator values were observed. The Euclidean distances are too small compared to MIP thin film channels. This channel has poor selectivity performance toward THC. For example, for the response of NIP thin film toward 400 ppm of methanol, ethanol, CBD, and THC, the relative response is 36.10%, 37.98%,

39.55%, and 40.95%, respectively, and the distance between THC and CBD were found to be 32.02.

MIP thin film 2 has showed the best performance considering the channel capability of THC recognition by observing the response graphs and the selectivity indicator values. The level and quality of the interaction with THC molecules is much higher and stronger than that of other analytes (methanol, ethanol, and CBD). The resistance drop because of THC exposure is much less than the decrease caused by methanol, ethanol, or CBD exposure. The selectivity indicator values were calculated. The Euclidean distances are greater, compared to NIP Thin Film channel. For example, 400 ppm, the distance between THC and CBD were 50.94 (59.11% increase). Besides, for 400 ppm of methanol, ethanol, and CBD, the relative response is 30.80% (15% decrease), 31.78% (16% decrease), and 26.97% (32% decrease), respectively. While for 400 ppm of THC, there is a decrease of about 50% in relative response (20.02%). The channel's sensitivity toward THC had 62.5% decrease, while it was 25% decrease for CBD, and roughly no change for methanol and ethanol. This was expected since CBD is the most similar molecule to THC among the investigated analytes, and the molecular shape and size of methanol and ethanol preclude them from interacting with the THC recognition sites, and even if they do, their interactions would be minimal. This suggests that the channel responses for MIP and NIP should not differ greatly from one another.

The response of MIP thin film 2 and NIP thin film channels to different concentrations (300 to 700 ppm) of THC, CBD, Ethanol, and Methanol can be seen in Figure 17 a), b), c), and d), respectively. The differences originate from MIP thin film cavities, and the interaction of these cavities with analytes is obvious. For MIP thin film 2 (compared to NIP channel), the decrease in

the resistance value of the sensor caused by analyte exposure is smaller for all concentrations of all analytes (methanol, ethanol, CBD, and THC).

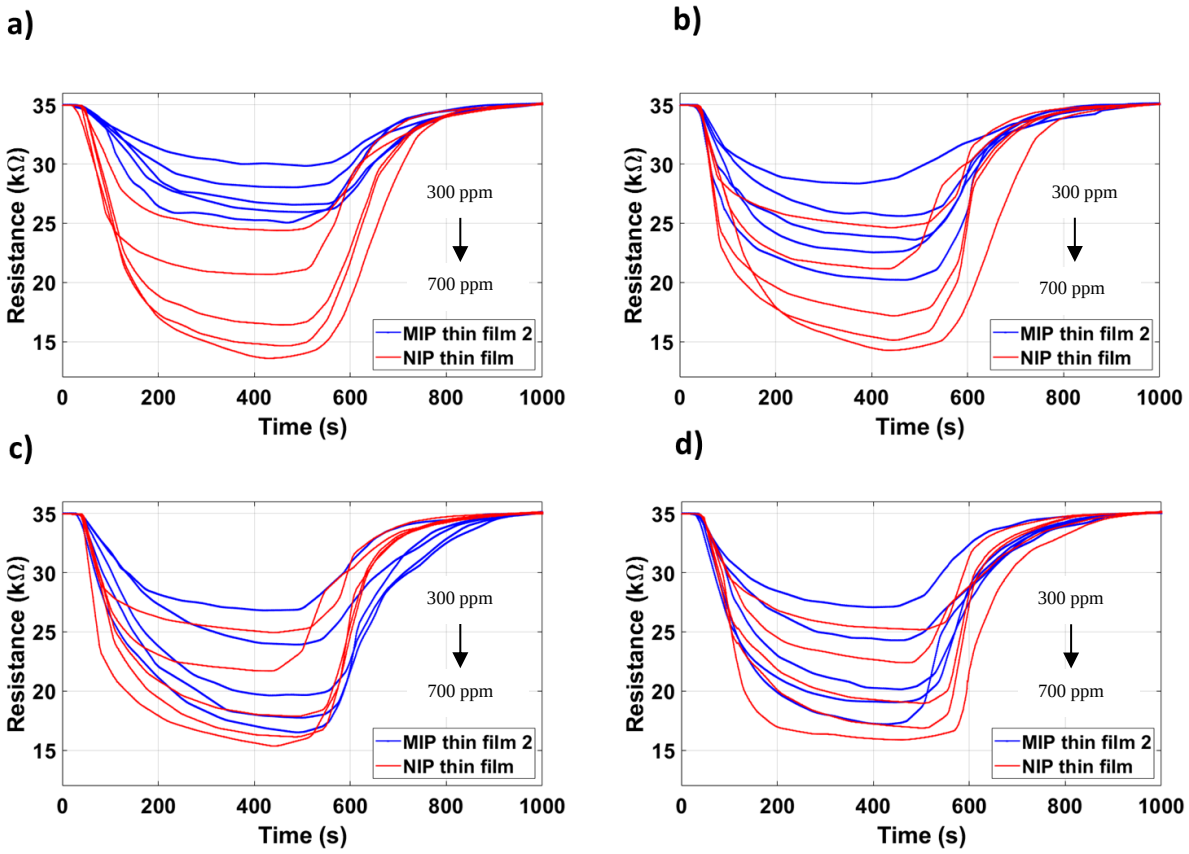

Figure 17 - The resistance versus time graphs for two channels upon exposure to five different concentrations (300 ppm–700 ppm) of a) THC, b) CBD, c) ethanol, d) methanol.

3.3 Statistical Analysis

Based on the results that obtained from gas sensing experiments, the properties of the microfluidic gas sensors, and the designed experiments, it is anticipated for the results to be sensitive to and determined by the concentration of the analyte, the analyte, and the coating of the channel. The effect of these three factors on the results were discussed thoroughly in the previous sections. Here, we want to ensure about the sensitivity of the results to these factors and the significance of these three factors using three-way ANOVA (analysis of variance) method in

MATLAB as a statistical analysis method. In this method, a significance level is decided as α=0.05. By calculating the p-value attributed to each factor, the significance of that factor can be obtained. The p-value is an indicator of the probability which is compared to the significance level (α). If the p-value of a factor is smaller than α, that factor is significant and the result is sensitive to the change of that factor.

For the NPs coated channels results, the p-values were calculated for the mentioned factors (the concentration of the analyte, the analyte, and the coating of the channel) and they were 2.39e-29, 6.76e-5, and 2.85e-9. All the p-values were dramatically smaller than α=0.05, indicating the significance of all the three factors and the sensitivity of the result to the change of these factors.

For the thin film coated channels, the calculated p-values were 7.89e-46, 7.87e-5, and 1.71e-29. Comparing to α=0.05, they were dramatically smaller. The mentioned three factors were significant and the result is sensitive to the change of these factors.

3.4 Classification

By observing the results obtained from MIP an NIP channels, it can be concluded that a dual MIP-NIP system seems ideal for selective detection using MOS based microfluidic device.

The data obtained from MIP and NIP NPs channels were combined, and the Fine KNN classification model available in MATLAB R2021b Classification Learner App was applied on this data to assess the capability to classify the data in four classes including THC, CBD, ethanol, and methanol.

The principal component analysis was applied on the data before classification, and the effect of number of principal components that were used is shown in Figure 18 a). By increasing the number of principal components, the best accuracy achieved with 4 of them. In Figure 18 b), the confusion matrix obtained from the classifier can be found. The classifier was able to do the

classification with an accuracy of 96.3%. The important class for us is the THC class, and the confusion between methanol and ethanol classes is negligible.

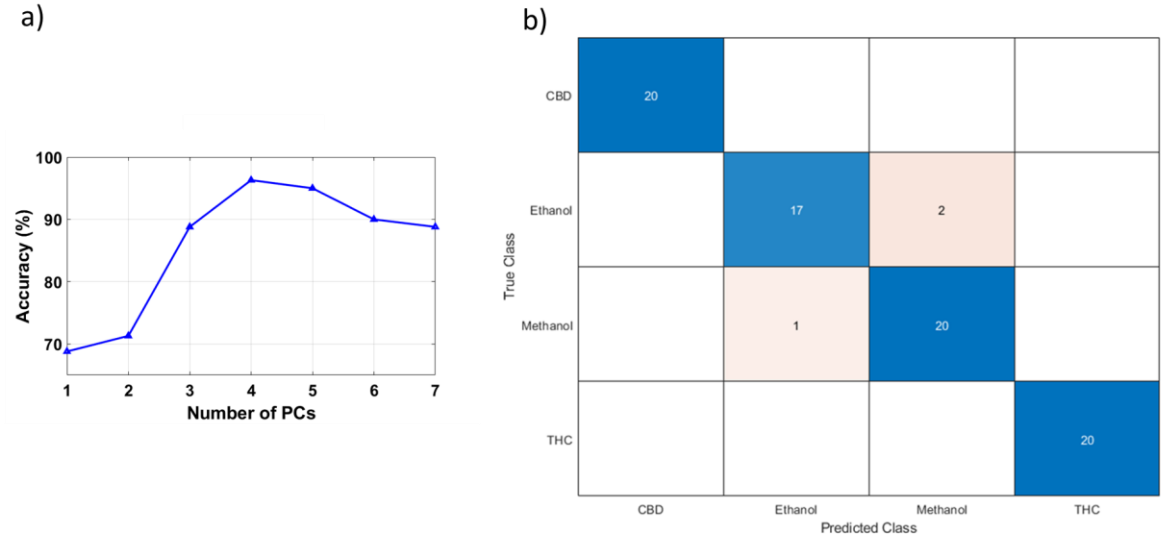

Figure 18 – a) Classification accuracy versus the number of used principal components, and b) The confusion matrix when the combined data from MIP and NIP NPs channels were used for the classification.

The same steps were taken for the MIP thin film 2 channel and NIP thin film channel. The best accuracy (100 %) achieved by using 3 or 4 principal components. In Figure 19 a) and b), the effect of number of principal components and the confusion matrix obtained by using 3 principal components can be found, respectively.

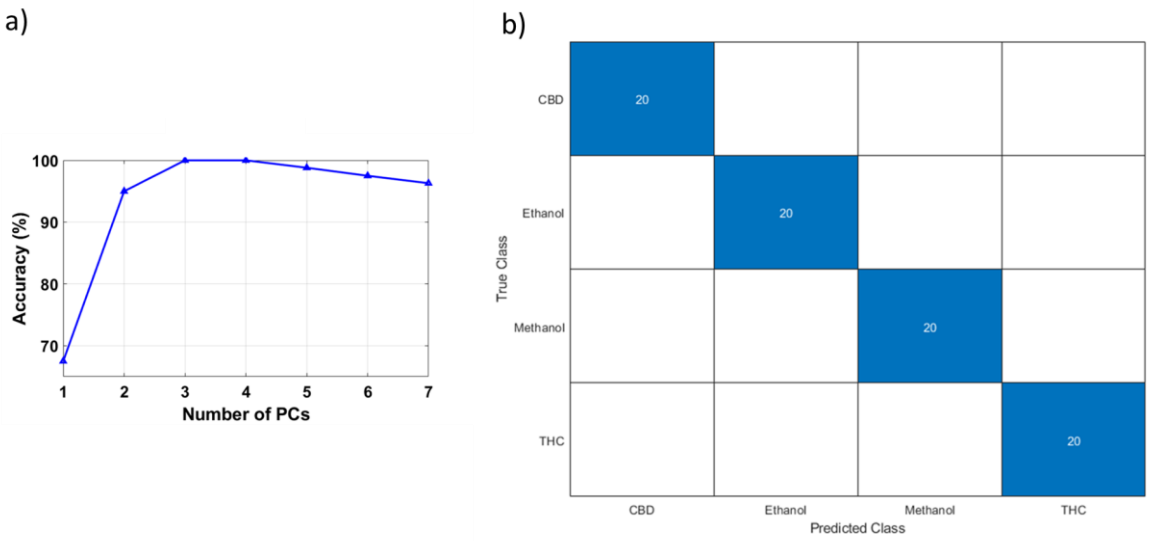

Figure 19 - a) Classification accuracy versus the number of used principal components, and b) The confusion matrix when the combined data from MIP thin film 2 and NIP thin film channels were used for the classification.

By taking a look at the elbow curve obtained for the NPs coated channels data (Figure 20 a), it can be said that the k=4 is the optimized k. The optimized k for the thin coated channels data is 4. It is obtained by observing the elbow curve of the data (Figure 20 b).

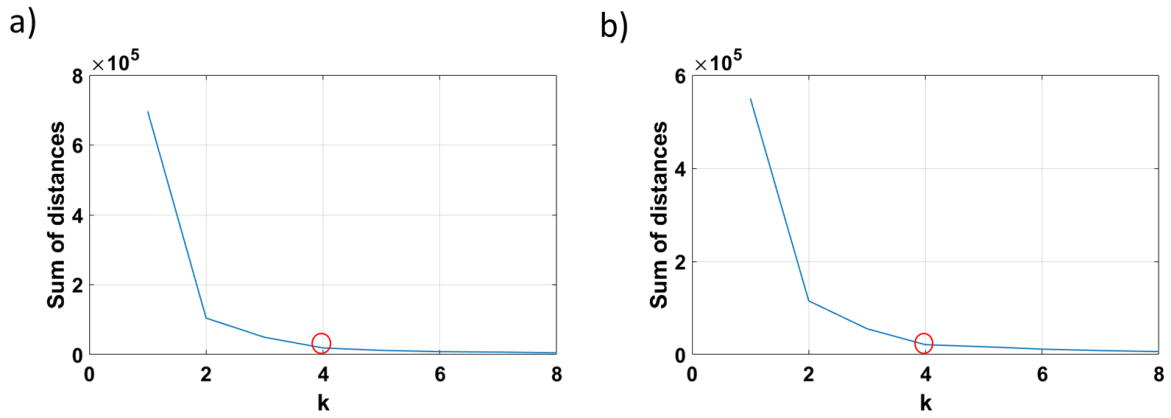

Figure 20 - Elbow curve for a) NPs coated channels data and b) thin film coated channels data

Chapter 4: Conclusion and future works

4.1 Conclusion

The ability to identify a THC sample is of utmost importance. The purpose of this study was to determine whether a given gas sample is a THC sample. The integration of THC MIPs and NIPs along with microfluidic devices (microfluidic channels and MOS sensors) made it possible to do so. The presence of THC recognition sites in the MIPs structure enhanced the selectivity of the channel toward THC.

In our first study, the MIP and NIP NPs were coated on the surface of two microfluidic channels. According to the responses and calculated parameters, the NIP NPs channel selectivity performance toward THC was poor while the MIP NPs channel was able to differentiate THC from CBD, methanol, and ethanol owing to the presence of THC recognition sites in MIP structure. By observing the difference between the responses of these two channels upon exposure to a gas sample, one can figure out whether a gas sample is a THC sample.

In our second study, three microfluidic channels were coated with MIP thin film, and one microfluidic channel was coated with NIP thin film. The only difference between the MIP thin film channels was the monomer (pyrrole): template (THC) ratio of the coated thin film. Among these three MIP thin film channels, one (MIP thin film 2) with the best selectivity performance toward THC was picked. By observing the difference between the responses of this channel and the NIP thin film channel, one can determine if a gas sample is a THC sample. Self-aggregation and a rise in the nonselective interaction of binding sites with analytes other than THC occurred at the channel (MIP thin film 1) with a higher monomer (pyrrole): template (THC) ratio. A lower ratio of pyrrole monomers to THC templates leads to poor assembly and an absence of suitable binding sites in the MIP thin film 3 channel.

Considering the data from both the MIP and NIP channels, it seems that a dual MIP-NIP system is the way to go for selective detection in a microfluidic device based on a MOS. The combined response data of MIP and NIP NPs channels were classified in four classes (THC, CBD, ethanol, and methanol) with 96.3% accuracy using the Fine KNN classification model available in MATLAB R2021b Classification Learner App. The same process and classification was done with the MIP thin film 2 and NIP thin film channels data successfully.

The results indicate that MIP and NIP NPs channels can be used together, and MIP and NIP thin film channels can be used together to successfully differentiate a THC gas sample from a methanol, ethanol, or CBD sample.

4.2 Future works

In this study, the feasibility of integration between MIPs, NIPs, microfluidic channels, and MOS sensors was shown to distinguish a THC sample from a methanol, ethanol, or CBD sample. Here, the thin film format and NPs format of MIPs were exposed to gases and tested separately. In each test, potential errors may be faced that vary from one test to another, such as the preparation of a gas sample. For future studies and precise comparison between MIP thin film and NPs performance, it is recommended to conduct a series of experiments containing both of them to be exposed simultaneously to gas samples. Also, it should be considered that in the thin film channels, a coating of chrome and gold existed between Parylene C coating and MIP thin film. While in the MIP NPs channel, there is no coating between Parylene C and MIP NPs. The presence of the layer of gold and chrome influences the interaction between analytes and the channel walls resulting in effects on the response and performance parameters. This is another factor that should be considered and studied for an accurate comparison between MIP thin film and NPs channels.

The performance and selectivity of the MIP-NIP thin film dual channel and MIP-NIP NPs dual channel can be studied and compared to each other. The MIP-NIP thin film dual channel and MIP-NIP NPs dual channel can be exposed to blend gas samples with more than one analyte in them to assess their capabilities and performance upon exposure to blend gas samples. The same devices can be fabricated for other analytes of interest by preparing the MIPs for that specific analyte.

Fabricating an array of MIP-NIP microchannel sensors for different analytes can be a good idea to benefit from a selective detection toward blend gas samples. In this case, this array would be capable of detecting different present analytes in a blend gas sample.

The sensitivity and selectivity of the developed devices can be tuned based on the specific application (e.g., extraction technologies or breath analysis). The MOS detector, the geometries of microchannel, the embedded microfeatures, the coatings of microchannel surface, and the thickness of MIP and NIP coating are some of the factors that can be changed to detect lower or higher concentrations.

The integration of MIPs with other gas detection methods, such as optical methods and electrochemical devices (e.g., interdigitated electrodes), can be studied. For example, MIP NPs synthesized in this study are not conductive, so they cannot be used as a coating on the surface of an interdigitated electrode (IDE) to fabricate an electrochemical sensor. To do so, MIP nanocomposites can be prepared. Then this prepared nanocomposite can be coated on an IDE as a conductive layer to fabricate a selective electrochemical device by the integration of MIP nanocomposites and IDEs.

MIPs’ compatibility with microfabrication technology is another potential research area so they can applied for portable and wearable THC sensing devices using blood, urine, saliva, and breath samples.

Bibliography

[1] J. Tan, Z. T. Jiang, R. Li, and X. P. Yan, "Molecularly-imprinted monoliths for sample treatment and separation," *TrAC Trends in Analytical Chemistry*, vol. 39, pp. 207–217, Oct. 2012, doi: 10.1016/J.TRAC.2012.05.009.

[2] M. P. Sooraj and A. S. Nair, "Molecularly imprinted polymer composites: Introduction and overview," *Molecularly Imprinted Polymer Composites: Synthesis, Characterisation and Applications*, pp. 1–3, Jan. 2021, doi: 10.1016/B978-0-12-819952-7.00011-1.

[3] B. Sellergren and A. J. Hall, "Molecularly Imprinted Polymers," *Supramol Chem*, Mar. 2012, doi: 10.1002/9780470661345.SMC137.

[4] Y. Cao, T. Feng, J. Xu, and C. Xue, "Recent advances of molecularly imprinted polymer-based sensors in the detection of food safety hazard factors," *Biosens Bioelectron*, vol. 141, p. 111447, Sep. 2019, doi: 10.1016/J.BIOS.2019.111447.

[5] J. J. Belbruno, "Molecularly Imprinted Polymers," *Chem Rev*, vol. 119, no. 1, pp. 94–119, Jan. 2019, doi: 10.1021/ACS.CHEMREV.8B00171/ASSET/IMAGES/MEDIUM/CR-2018-00171R_0011.GIF.

[6] G. Vasapollo *et al.*, "Molecularly Imprinted Polymers: Present and Future Prospective," *International Journal of Molecular Sciences 2011, Vol. 12, Pages 5908-5945*, vol. 12, no. 9, pp. 5908–5945, Sep. 2011, doi: 10.3390/IJMS12095908.

[7] C. Alexander *et al.*, "Molecular imprinting science and technology: a survey of the literature for the years up to and including 2003," *Journal of Molecular Recognition*, vol. 19, no. 2, pp. 106–180, Mar. 2006, doi: 10.1002/JMR.760.

[8] A. A. Ensafi and P. Nasr-Esfahani, “Fundamental aspects of molecular imprinting,” *Molecularly Imprinted Polymer Composites: Synthesis, Characterisation and Applications*, pp. 5–20, Jan. 2021, doi: 10.1016/B978-0-12-819952-7.00008-1.

[9] F. Deng, X. B. Luo, L. Ding, and S. L. Luo, “Application of Nanomaterials and Nanotechnology in the Reutilization of Metal Ion From Wastewater,” *Nanomaterials for the Removal of Pollutants and Resource Reutilization*, pp. 149–178, Jan. 2019, doi: 10.1016/B978-0-12-814837-2.00005-6.

[10] S. Janfaza *et al.*, “A Nanostructured Microfluidic Artificial Olfaction for Organic Vapors Recognition,” *Scientific Reports 2019 9:1*, vol. 9, no. 1, pp. 1–8, Dec. 2019, doi: 10.1038/s41598-019-55672-z.

[11] S. Haghdoust and P. A. Lieberzeit, “P2BM.5 - Synthesis of a Novel MIP Thin Layer and Monodisperse MIP- Nanoparticles for Detection of Creatinine,” *Proceedings IMCS 2018*, pp. 694–695, Jul. 2018, doi: 10.5162/IMCS2018/P2BM.5.

[12] A. Lamaoui, J. J. García-Guzmán, A. Amine, J. M. Palacios-Santander, and L. Cubillana-Aguilera, “Synthesis techniques of molecularly imprinted polymer composites,” *Molecularly Imprinted Polymer Composites: Synthesis, Characterisation and Applications*, pp. 49–91, Jan. 2021, doi: 10.1016/B978-0-12-819952-7.00002-0.

[13] J. Mazuryk, P. S. Sharma, and W. Kutner, “Molecularly imprinted polymer composites in drug delivery,” *Molecularly Imprinted Polymer Composites: Synthesis, Characterisation and Applications*, pp. 173–226, Jan. 2021, doi: 10.1016/B978-0-12-819952-7.00014-7.

[14] A. Yarman, S. Kurbanoglu, K. J. Jetzschmann, S. A. Ozkan, U. Wollenberger, and F. W. Scheller, “Electrochemical MIP-Sensors for Drugs,” *Curr Med Chem*, vol. 25, no. 33, pp. 4007–4019, Oct. 2017, doi: 10.2174/0929867324666171005103712.

[15] R. D. Crapnell *et al.*, “Recent Advances in Electrosynthesized Molecularly Imprinted Polymer Sensing Platforms for Bioanalyte Detection,” *Sensors 2019, Vol. 19, Page 1204*, vol. 19, no. 5, p. 1204, Mar. 2019, doi: 10.3390/S19051204.

[16] B. E. Georgescu *et al.*, “Application of unusual on/off electrochemical properties of a molecularly imprinted polymer based on an EDOT–thiophene precursor for the detection of ephedrine,” *Electrochem commun*, vol. 94, pp. 45–48, Sep. 2018, doi: 10.1016/J.ELECOM.2018.08.004.

[17] A. Gonzalez-Vogel, A. Fogde, C. Crestini, T. Sandberg, T. P. Huynh, and J. Bobacka, “Molecularly imprinted conducting polymer for determination of a condensed lignin marker,” *Sens Actuators B Chem*, vol. 295, pp. 186–193, Sep. 2019, doi: 10.1016/J.SNB.2019.05.011.

[18] P. Lach, P. S. Sharma, K. Golebiewska, M. Cieplak, F. D’Souza, and W. Kutner, “Molecularly Imprinted Polymer Chemosensor for Selective Determination of an N-Nitroso-l-proline Food Toxin,” *Chemistry – A European Journal*, vol. 23, no. 8, pp. 1942–1949, Feb. 2017, doi: 10.1002/CHEM.201604799.

[19] A. R. Koohpaei, S. J. Shahtaheri, M. R. Ganjali, A. R. Forushani, and F. Golbabaei, “Application of multivariate analysis to the screening of molecularly imprinted polymers (MIPs) for ametryn,” *Talanta*, vol. 75, no. 4, pp. 978–986, May 2008, doi: 10.1016/J.TALANTA.2007.12.046.

[20] A. Ait Lahcen, F. Arduini, F. Lista, and A. Amine, “Label-free electrochemical sensor based on spore-imprinted polymer for Bacillus cereus spore detection,” *Sens Actuators B Chem*, vol. 276, pp. 114–120, Dec. 2018, doi: 10.1016/J.SNB.2018.08.031.

[21] D. Capoferri *et al.*, “MIP-MEPS based sensing strategy for the selective assay of dimethoate. Application to wheat flour samples,” *Talanta*, vol. 174, pp. 599–604, Nov. 2017, doi: 10.1016/J.TALANTA.2017.06.062.

[22] S. Jafari, M. Dehghani, N. Nasirizadeh, and M. Azimzadeh, “An azithromycin electrochemical sensor based on an aniline MIP film electropolymerized on a gold nano urchins/graphene oxide modified glassy carbon electrode,” *Journal of Electroanalytical Chemistry*, vol. 829, pp. 27–34, Nov. 2018, doi: 10.1016/J.JELECHEM.2018.09.053.

[23] A. K. Roy, V. S. Nisha, C. Dhand, and B. D. Malhotra, “Molecularly imprinted polyaniline film for ascorbic acid detection,” *Journal of Molecular Recognition*, vol. 24, no. 4, pp. 700–706, Jul. 2011, doi: 10.1002/JMR.1104.

[24] P. Liu, X. Zhang, W. Xu, C. Guo, and S. Wang, “Electrochemical sensor for the determination of brucine in human serum based on molecularly imprinted poly-o-phenylenediamine/SWNTs composite film,” *Sens Actuators B Chem*, vol. 163, no. 1, pp. 84–89, Mar. 2012, doi: 10.1016/J.SNB.2012.01.011.

[25] D. C. Apodaca, R. B. Pernites, R. Ponnapati, F. R. del Mundo, and R. C. Advincula, “Electropolymerized molecularly imprinted polymer film: EIS sensing of bisphenol A,” *Macromolecules*, vol. 44, no. 17, pp. 6669–6682, Sep. 2011, doi: 10.1021/MA2010525/SUPPL_FILE/MA2010525_SI_001.PDF.

[26] P. S. Sharma, A. Pietrzyk-Le, F. D’Souza, and W. Kutner, “Electrochemically synthesized polymers in molecular imprinting for chemical sensing,” *Analytical and Bioanalytical Chemistry 2012 402:10*, vol. 402, no. 10, pp. 3177–3204, Feb. 2012, doi: 10.1007/S00216-011-5696-6.

[27] S. Sadki, P. Schottland, N. Brodie, and G. Sabouraud, “The mechanisms of pyrrole electropolymerization,” *Chem Soc Rev*, vol. 29, no. 5, pp. 283–293, Jan. 2000, doi: 10.1039/A807124A.

[28] A. A. Ensafi, N. Kazemifard, and Z. Saberi Dehkordi, “Parameters that affect molecular imprinting polymers,” *Molecularly Imprinted Polymer Composites: Synthesis, Characterisation and Applications*, pp. 21–48, Jan. 2021, doi: 10.1016/B978-0-12-819952-7.00010-X.

[29] “Molecularly Imprinted Sensors: Overview and Applications - Google Books.” https://books.google.ca/books?hl=en&lr=&id=VkAfzfsYpisC&oi=fnd&pg=PP2&ots=eWwG20ay6G&sig=EqqCy5AMBCekqTgPMVcK_9duP0g&redir_esc=y#v=onepage&q&f=false (accessed Oct. 16, 2022).

[30] H. S. Andersson, J. G. Karlsson, S. A. Piletsky, A. C. Koch-Schmidt, K. Mosbach, and I. A. Nicholls, “Study of the nature of recognition in molecularly imprinted polymers, II : Influence of monomer–template ratio and sample load on retention and selectivity,” *J Chromatogr A*, vol. 848, no. 1–2, pp. 39–49, Jul. 1999, doi: 10.1016/S0021-9673(99)00483-5.

[31] B. Mortari, S. Zeb, R. R. Pupin, S. Khan, A. Wong, and M. D. P. T. Sotomayor, “Molecularly imprinted polymer composites as sensor,” *Molecularly Imprinted Polymer Composites: Synthesis, Characterisation and Applications*, pp. 227–265, Jan. 2021, doi: 10.1016/B978-0-12-819952-7.00012-3.

[32] P. Tong, M. Li, Y. Meng, and J. Li, “Molecularly imprinted polymer composites in biological analysis,” *Molecularly Imprinted Polymer Composites: Synthesis,*

Characterisation and Applications, pp. 143–172, Jan. 2021, doi: 10.1016/B978-0-12-819952-7.00001-9.

[33] C. K. HO, M. T. ITAMURA, M. J. KELLEY, and R. C. HUGHES, "Review of Chemical Sensors for In-Situ Monitoring of Volatile Contaminants," *Contract*, vol. 2001, no. March, p. 34, Mar. 2001, doi: 10.2172/780299.

[34] M. McGrath and C. Scanaill, *Sensor technologies: healthcare, wellness, and environmental applications*. 2013. Accessed: Oct. 17, 2022. [Online]. Available: https://library.oapen.org/bitstream/handle/20.500.12657/28153/1001841.pdf?sequence=1

[35] M. Majdinasab, K. Mitsubayashi, and J. L. Marty, "Optical and Electrochemical Sensors and Biosensors for the Detection of Quinolones," *Trends Biotechnol*, vol. 37, no. 8, pp. 898–915, Aug. 2019, doi: 10.1016/J.TIBTECH.2019.01.004.

[36] F. R. Baptista, S. A. Belhout, S. Giordani, and S. J. Quinn, "Recent developments in carbon nanomaterial sensors," *Chem Soc Rev*, vol. 44, no. 13, pp. 4433–4453, Jun. 2015, doi: 10.1039/C4CS00379A.

[37] G. Yang, F. Zhao, and B. Zeng, "Electrochemical determination of cefotaxime based on a three-dimensional molecularly imprinted film sensor," *Biosens Bioelectron*, vol. 53, pp. 447–452, Mar. 2014, doi: 10.1016/J.BIOS.2013.10.029.

[38] T. Khumsap and L. T. Nguyen, "Molecularly imprinted polymer composites for detecting toxic contaminants in agricultural products," *Molecularly Imprinted Polymer Composites: Synthesis, Characterisation and Applications*, pp. 309–344, Jan. 2021, doi: 10.1016/B978-0-12-819952-7.00009-3.

[39] B. Si and E. Song, “Molecularly imprinted polymers for the selective detection of multi-analyte neurotransmitters,” *Microelectron Eng*, vol. 187–188, pp. 58–65, Feb. 2018, doi: 10.1016/J.MEE.2017.11.016.

[40] H. F. Hawari *et al.*, “Array of MIP-Based Sensor for Fruit Maturity Assessment,” *Procedia Chem*, vol. 6, pp. 100–109, 2012, doi: 10.1016/j.proche.2012.10.135.

[41] R. Li, Y. Feng, G. Pan, and L. Liu, “Advances in Molecularly Imprinting Technology for Bioanalytical Applications,” *Sensors 2019, Vol. 19, Page 177*, vol. 19, no. 1, p. 177, Jan. 2019, doi: 10.3390/S19010177.

[42] M. Mousazadeh *et al.*, “Detection of hexanal gas as a volatile organic compound cancer biomarker using a nanocomposite of gold nanoparticles and selective polymers,” *Journal of Electroanalytical Chemistry*, vol. 905, p. 115962, Jan. 2022, doi: 10.1016/J.JELECHEM.2021.115962.

[43] A. Jahangiri-Manesh, M. Mousazadeh, and M. Nikkhah, “Fabrication of chemiresistive nanosensor using molecularly imprinted polymers for acetone detection in gaseous state,” *Iranian Polymer Journal (English Edition)*, vol. 31, no. 7, pp. 883–891, Jul. 2022, doi: 10.1007/S13726-022-01044-W/TABLES/2.

[44] S. Janfaza *et al.*, “A selective chemiresistive sensor for the cancer-related volatile organic compound hexanal by using molecularly imprinted polymers and multiwalled carbon nanotubes”, doi: 10.1007/s00604-019-3241-z.

[45] S. Piletsky and A. Turner, “Electrochemical sensors based on molecularly imprinted polymers,” *Electroanalysis*, vol. 14, no. 5, pp. 317–323, 2002, Accessed: Oct. 17, 2022. [Online]. Available: http://urn.kb.se/resolve?urn=urn:nbn:se:liu:diva-65215

[46] D. Lakshmi *et al.*, “Electrochemical sensor for catechol and dopamine based on a catalytic molecularly imprinted polymer-conducting polymer hybrid recognition element,” *Anal Chem*, vol. 81, no. 9, pp. 3576–3584, May 2009, doi: 10.1021/AC802536P/SUPPL_FILE/AC802536P_SI_001.PDF.

[47] V. Suryanarayanan, C. T. Wu, and K. C. Ho, “Molecularly Imprinted Electrochemical Sensors,” *Electroanalysis*, vol. 22, no. 16, pp. 1795–1811, Aug. 2010, doi: 10.1002/ELAN.200900616.

[48] R. Galassi, C. Contini, M. Pucci, E. Gambi, and G. Manca, “Odorant Monitoring in Natural Gas Pipelines Using Ultraviolet-Visible Spectroscopy,” *Appl Spectrosc*, vol. 75, no. 2, pp. 168–177, Feb. 2021, doi: 10.1177/0003702820960737.

[49] S. v. Kireev, S. L. Shnyrev, S. v. Kireev, and S. L. Shnyrev, “On-line monitoring of odorant in natural gas mixtures of different composition by the infrared absorption spectroscopy method,” *LaPhL*, vol. 15, no. 3, p. 035705, Mar. 2018, doi: 10.1088/1612-202X/AA9D9F.

[50] S. W. Myung *et al.*, “Gas chromatographic-mass spectrometric analysis of mercaptan odorants in liquefied petroleum gas and liquefied natural gas,” *J Chromatogr A*, vol. 791, no. 1–2, pp. 367–370, Dec. 1997, doi: 10.1016/S0021-9673(97)00843-1.

[51] C. D. Pearson, “The determination of trace mercaptans and sulfides in natural gas by a gas chromatography-flame photometric detector technique,” *J Chromatogr Sci*, vol. 14, no. 3, pp. 154–158, 1976, doi: 10.1093/CHROMSCI/14.3.154.

[52] J. Hodgkinson and R. P. Tatam, “Optical gas sensing: a review,” *Meas Sci Technol*, vol. 24, no. 1, p. 012004, Nov. 2012, doi: 10.1088/0957-0233/24/1/012004.

[53] K. Länge, B. E. Rapp, and M. Rapp, “Surface acoustic wave biosensors: a review,” *Anal Bioanal Chem*, vol. 391, no. 5, pp. 1509–1519, Jul. 2008, doi: 10.1007/S00216-008-1911-5.

[54] A. Mirzaei, S. S. Kim, and H. W. Kim, “Resistance-based H2S gas sensors using metal oxide nanostructures: A review of recent advances,” *J Hazard Mater*, vol. 357, pp. 314–331, Sep. 2018, doi: 10.1016/J.JHAZMAT.2018.06.015.

[55] S. Zhao *et al.*, “Complex-surfactant-assisted hydrothermal synthesis of one-dimensional ZnO nanorods for high-performance ethanol gas sensor,” *Sens Actuators B Chem*, vol. 286, pp. 501–511, May 2019, doi: 10.1016/J.SNB.2019.01.127.

[56] Z. Li *et al.*, “Room-Temperature High-Performance H2S Sensor Based on Porous CuO Nanosheets Prepared by Hydrothermal Method,” *ACS Appl Mater Interfaces*, vol. 8, no. 32, pp. 20962–20968, Aug. 2016, doi: 10.1021/ACSAMI.6B02893/SUPPL_FILE/AM6B02893_SI_001.PDF.

[57] J. H. Bang *et al.*, “Porous Si/SnO2 nanowires heterostructures for H2S gas sensing,” *Ceram Int*, vol. 46, no. 1, pp. 604–611, Jan. 2020, doi: 10.1016/J.CERAMINT.2019.09.010.

[58] V. E. Henrich and P. A. Cox, “The surface science of metal oxides,” p. 464, 1994.

[59] A. Afzal, N. Cioffi, L. Sabbatini, and L. Torsi, “NO x sensors based on semiconducting metal oxide nanostructures: Progress and perspectives,” *Sens Actuators B Chem*, vol. 171–172, pp. 25–42, Aug. 2012, doi: 10.1016/J.SNB.2012.05.026.

[60] G. Eranna, *Metal Oxide Nanostructures As Gas Sensing Devices (Series in Sensors)*. Accessed: Oct. 17, 2022. [Online]. Available: https://www.routledge.com/Metal-Oxide-Nanostructures-as-Gas-Sensing-Devices/Eranna/p/book/9780367381868

[61] A. Mirzaei, S. G. Leonardi, and G. Neri, “Detection of hazardous volatile organic compounds (VOCs) by metal oxide nanostructures-based gas sensors: A review,” *Ceram Int*, vol. 42, no. 14, pp. 15119–15141, Nov. 2016, doi: 10.1016/J.CERAMINT.2016.06.145.

[62] N. Barsan and K. Schierbaum, “Gas sensors based on conducting metal oxides: Basic understanding, technology and applications,” *Gas Sensors Based on Conducting Metal Oxides: Basic Understanding, Technology and Applications*, pp. 1–269, Jan. 2018, doi: 10.1016/C2016-0-00984-1.

[63] M. A. Carpenter, Sanjay. Mathur, and Andrei. Kolmakov, “Metal oxide nanomaterials for chemical sensors,” 2013.

[64] A. Afzal and F. L. Dickert, “Imprinted Oxide and MIP/Oxide Hybrid Nanomaterials for Chemical Sensors †,” *Nanomaterials 2018, Vol. 8, Page 257*, vol. 8, no. 4, p. 257, Apr. 2018, doi: 10.3390/NANO8040257.

[65] F. Hossein-Babaei, A. Hooshyar Zare, V. Ghafarinia, and S. Erfantalab, “Identifying volatile organic compounds by determining their diffusion and surface adsorption parameters in microfluidic channels,” *Sens Actuators B Chem*, vol. 220, pp. 607–613, Dec. 2015, doi: 10.1016/J.SNB.2015.06.014.

[66] F. Hossein-Babaei, A. Hooshyar Zare, and V. Ghafarinia, “Transient molecular diffusion in microfluidic channels: Modeling and experimental verification of the results,” *Sens Actuators B Chem*, vol. 233, pp. 646–653, Oct. 2016, doi: 10.1016/J.SNB.2016.04.103.

[67] M. Paknahad, J. S. Bachhal, A. Ahmadi, and M. Hoorfar, “Characterization of channel coating and dimensions of microfluidic-based gas detectors,” *Sens Actuators B Chem*, vol. 241, pp. 55–64, Mar. 2017, doi: 10.1016/J.SNB.2016.10.048.

[68] M. Paknahad, C. Mcintosh, and M. Hoorfar, “Selective detection of volatile organic compounds in microfluidic gas detectors based on ‘like dissolves like,’” *Scientific Reports 2019 9:1*, vol. 9, no. 1, pp. 1–11, Jan. 2019, doi: 10.1038/s41598-018-36615-6.

[69] M. Pumera, J. Wang, E. Grushka, and R. Polsky, “Gold Nanoparticle-Enhanced Microchip Capillary Electrophoresis,” 2001, doi: 10.1021/ac015589e.

[70] M. Ghazi, S. Janfaza, H. Tahmooressi, N. Tasnim, and M. Hoorfar, “Selective detection of VOCs using microfluidic gas sensor with embedded cylindrical microfeatures coated with graphene oxide,” *J Hazard Mater*, vol. 424, p. 127566, Feb. 2022, doi: 10.1016/J.JHAZMAT.2021.127566.

[71] Q. Yang, J. Li, X. Wang, H. Peng, H. Xiong, and L. Chen, “Strategies of molecular imprinting-based fluorescence sensors for chemical and biological analysis,” *Biosens Bioelectron*, vol. 112, pp. 54–71, Jul. 2018, doi: 10.1016/J.BIOS.2018.04.028.

[72] J. Liu *et al.*, “Electrochemical microfluidic chip based on molecular imprinting technique applied for therapeutic drug monitoring,” *Biosens Bioelectron*, vol. 91, pp. 714–720, May 2017, doi: 10.1016/J.BIOS.2017.01.037.

[73] L. Chen, X. Wang, W. Lu, X. Wu, and J. Li, “Molecular imprinting: perspectives and applications,” *Chem Soc Rev*, vol. 45, no. 8, pp. 2137–2211, Apr. 2016, doi: 10.1039/C6CS00061D.

[74] F. Grotenhermen and E. Russo, “Cannabis and Cannabinoids: Pharmacology, Toxicology, and Therapeutic Potential,” *Cannabis and Cannabinoids: Pharmacology, Toxicology, and Therapeutic Potential*, pp. 1–439, Sep. 2013, doi: 10.4324/9780203479506.

[75] “Global overview of drug demand and supply,” pp. 1–60, Jun. 2018, doi: 10.18356/3A4C2E67-EN.

[76] H. Mirzaei, A. O'Brien, N. Tasnim, A. Ravishankara, H. Tahmooressi, and M. Hoorfar, "Topical review on monitoring tetrahydrocannabinol in breath," *J Breath Res*, vol. 14, no. 3, Jul. 2020, doi: 10.1088/1752-7163/AB6229.

[77] G. Battistella *et al.*, "Long-Term Effects of Cannabis on Brain Structure," *Neuropsychopharmacology 2014 39:9*, vol. 39, no. 9, pp. 2041–2048, Mar. 2014, doi: 10.1038/npp.2014.67.

[78] M. A. Huestis, "Deterring driving under the influence of cannabis," *Addiction*, vol. 110, no. 11, pp. 1697–1698, Nov. 2015, doi: 10.1111/ADD.13041.

[79] R. L. Hartman *et al.*, "Cannabis effects on driving longitudinal control with and without alcohol," *Journal of Applied Toxicology*, vol. 36, no. 11, pp. 1418–1429, Nov. 2016, doi: 10.1002/JAT.3295.

[80] M. Huestis, "Cannabis (Marijuana) - Effects on Human Performance and Behavior.," *undefined*, 2002.

[81] P. Yáñez-Sedenõ, L. Agui, S. Campuzano, and J. M. Pingarrón, "What Electrochemical Biosensors Can Do for Forensic Science? Unique Features and Applications," *Biosensors (Basel)*, vol. 9, no. 4, 2019, doi: 10.3390/BIOS9040127.

[82] J. Sánchez-González, R. Salgueiro-Fernández, P. Cabarcos, A. M. Bermejo, P. Bermejo-Barrera, and A. Moreda-Piñeiro, "Cannabinoids assessment in plasma and urine by high performance liquid chromatography-tandem mass spectrometry after molecularly imprinted polymer microsolid-phase extraction," *Anal Bioanal Chem*, vol. 409, no. 5, pp. 1207–1220, Feb. 2017, doi: 10.1007/S00216-016-0046-3.

[83] M. Nestić, S. Babić, D. M. Pavlović, and D. Sutlović, "Molecularly imprinted solid phase extraction for simultaneous determination of Δ9-tetrahydrocannabinol and its main

metabolites by gas chromatography-mass spectrometry in urine samples," *Forensic Sci Int*, vol. 231, no. 1–3, pp. 317–324, Sep. 2013, doi: 10.1016/J.FORSCIINT.2013.06.009.

[84] Q. Zhang, D. Berg, and S. M. Mugo, "Molecularly imprinted carbon based electrodes for tetrahydrocannabinol sensing," *Inorg Chem Commun*, vol. 107, p. 107459, Sep. 2019, doi: 10.1016/J.INOCHE.2019.107459.

[85] M. Paknahad, J. S. Bachhal, A. Ahmadi, and M. Hoorfar, "Highly selective multi-target 3D-printed microfluidic-based breath analyzer," *Proceedings of the IEEE International Conference on Micro Electro Mechanical Systems (MEMS)*, vol. 2016-February, pp. 905–908, Feb. 2016, doi: 10.1109/MEMSYS.2016.7421777.

[86] M. Paknahad, "Development of highly selective single sensor microfluidic-based gas detector," 2017, doi: 10.14288/1.0357368.

[87] M. Paknahad, J. S. Bachhal, and M. Hoorfar, "Diffusion-based humidity control membrane for microfluidic-based gas detectors," *Anal Chim Acta*, vol. 1021, pp. 103–112, Aug. 2018, doi: 10.1016/J.ACA.2018.03.021.

[88] V. Ghafarinia, A. Amini, and M. Paknahad, "Gas identification by a single gas sensor equipped with microfluidic channels," *Sens Lett*, vol. 10, no. 3–4, pp. 845–849, Mar. 2012, doi: 10.1166/SL.2012.2590.

[89] M. Paknahad, A. Ahmadi, J. Rousseau, H. R. Nejad, and M. Hoorfar, "On-Chip Electronic Nose For Wine Tasting: A Digital Microfluidic Approach," *IEEE Sens J*, vol. 17, no. 14, pp. 4322–4329, Jul. 2017, doi: 10.1109/JSEN.2017.2707525.

[90] H. J. Leamy, "Charge collection scanning electron microscopy," *J Appl Phys*, vol. 53, no. 6, p. R51, Jun. 1998, doi: 10.1063/1.331667.

[91] J. I. Goldstein, D. E. Newbury, J. R. Michael, N. W. M. Ritchie, J. H. J. Scott, and D. C. Joy, “Scanning electron microscopy and x-ray microanalysis,” *Scanning Electron Microscopy and X-ray Microanalysis*, pp. 1–550, Jan. 2017, doi: 10.1007/978-1-4939-6676-9/COVER.

[92] W. Zhou, R. Apkarian, Z. L. Wang, and D. Joy, “Fundamentals of scanning electron microscopy (SEM),” *Scanning Microscopy for Nanotechnology: Techniques and Applications*, pp. 1–40, 2007, doi: 10.1007/978-0-387-39620-0_1.

[93] D. E. Newbury, D. C. Joy, Patrick. Echlin, C. E. Fiori, and J. Goldstein, “Advanced Scanning Electron Microscopy and X-Ray Microanalysis,” p. 454, 1986.

[94] C. S. Fadley, “X-ray photoelectron spectroscopy: Progress and perspectives,” *J Electron Spectros Relat Phenomena*, vol. 178–179, no. C, pp. 2–32, May 2010, doi: 10.1016/J.ELSPEC.2010.01.006.

[95] J. M. Hollander and W. L. Jolly, “X-Ray Photoelectron Spectroscopy,” *Acc Chem Res*, vol. 3, no. 6, pp. 193–200, Jun. 1970, doi: 10.1021/AR50030A003/ASSET/AR50030A003.FP.PNG_V03.

[96] J. Moulder, W. Stickle, W. Sobol, and K. D. Bomben, “Handbook of X-Ray Photoelectron Spectroscopy,” *undefined*, 1992.

[97] “D. A. Long, ‘Raman Spectroscopy’ McGraw-Hill, New York, 1977. - References - Scientific Research Publishing.” https://www.scirp.org/(S(351jmbntvnsjt1aadkozje))/reference/referencespapers.aspx?referenceid=921080 (accessed Oct. 18, 2022).

[98] C. v. Raman and K. S. Krishnan, “Polarisation of Scattered Light-quanta,” *Nature 1928 122:3066*, vol. 122, no. 3066, pp. 169–169, 1928, doi: 10.1038/122169a0.

[99] E. v. Efremov, F. Ariese, and C. Gooijer, “Achievements in resonance Raman spectroscopy review of a technique with a distinct analytical chemistry potential,” *Anal Chim Acta*, vol. 606, no. 2, pp. 119–134, Jan. 2008, doi: 10.1016/J.ACA.2007.11.006.

[100] R. S. Das and Y. K. Agrawal, “Raman spectroscopy: Recent advancements, techniques and applications,” *Vib Spectrosc*, vol. 57, no. 2, pp. 163–176, Nov. 2011, doi: 10.1016/J.VIBSPEC.2011.08.003.

[101] E. C. Y. Li-Chan, “The applications of Raman spectroscopy in food science,” *Trends Food Sci Technol*, vol. 11, no. 7, pp. 361–370, 1996, Accessed: Oct. 18, 2022. [Online]. Available: https://www.infona.pl//resource/bwmeta1.element.elsevier-7c09468b-bdda-332f-b641-770ae3d5f2a5

[102] “(PDF) Raman Spectroscopy, a review.” https://www.researchgate.net/publication/309179824_Raman_Spectroscopy_a_review (accessed Oct. 18, 2022).

[103] V. S. Bhati *et al.*, “Improved Sensitivity with Low Limit of Detection of a Hydrogen Gas Sensor Based on rGO-Loaded Ni-Doped ZnO Nanostructures,” *ACS Appl Mater Interfaces*, vol. 10, no. 13, pp. 11116–11124, Apr. 2018, doi: 10.1021/ACSAMI.7B17877.

[104] R. Kumar, N. Goel, and M. Kumar, “UV-Activated MoS2 Based Fast and Reversible NO2 Sensor at Room Temperature,” *ACS Sens*, vol. 2, no. 11, pp. 1744–1752, Nov. 2017, doi: 10.1021/ACSSENSORS.7B00731.

[105] M. Ghazi, N. Tasnim, and M. Hoorfar, “Selective monitoring of natural gas sulphur-based odorant mixture of t-butyl mercaptan and methyl ethyl sulphide using an array of microfluidic gas sensors,” *J Hazard Mater*, vol. 438, p. 129548, Sep. 2022, doi: 10.1016/J.JHAZMAT.2022.129548.

[106] J. H. Choi, H. Kim, H. K. Sung, and H. Y. Cha, “Investigation of Stability and Power Consumption of an AlGaN/GaN Heterostructure Hydrogen Gas Sensor Using Different Bias Conditions,” *Sensors 2019, Vol. 19, Page 5549*, vol. 19, no. 24, p. 5549, Dec. 2019, doi: 10.3390/S19245549.

[107] I. Jolliffe, “Principal Component Analysis,” *Encyclopedia of Statistics in Behavioral Science*, Oct. 2005, doi: 10.1002/0470013192.BSA501.

[108] M. S. Landis, J. P. Pancras, J. R. Graney, R. K. Stevens, K. E. Percy, and S. Krupa, “Receptor Modeling of Epiphytic Lichens to Elucidate the Sources and Spatial Distribution of Inorganic Air Pollution in the Athabasca Oil Sands Region,” *Developments in Environmental Science*, vol. 11, pp. 427–467, Jan. 2012, doi: 10.1016/B978-0-08-097760-7.00018-4.